FOSSIL ENERGY

DOE/BC/15135-2
(OSTI ID: 790863)

CALIBRATION OF SEISMIC ATTRIBUTES FOR RESERVOIR CHARACTERIZATION

Annual Report
October 1, 2000-September 30, 2001

By:
Wayne D. Pennington
Horacio Acevedo
Aaron Green
Shawn Len
Anastasia Minaeva
James Wood
Deyi Xie

Date Published: January 2002

Work Performed Under Contract No. DE-AC26-98BC15135

Michigan Technological University
Houghton, Michigan

National Energy Technology Laboratory
National Petroleum Technology Office
U.S. DEPARTMENT OF ENERGY
Tulsa, Oklahoma

DOE/BC/15135-2
Distribution Category UC-122

Calibration of Seismic Attributes for Reservoir Characterization

By
Wayne D. Pennington
Horacio Acevedo
Aaron Green
Shawn Len
Anastasia Minaeva
James Wood
Deyi Xie

January 2002

Work Performed Under DE-AC26-98BC15135

Prepared for
U.S. Department of Energy
Assistant Secretary for Fossil Energy

Purna Halder, Project Manager
National Petroleum Technology Office
P.O. Box 3628
Tulsa, OK 74101

Prepared by
Department of Geological Engineering and Sciences
Michigan Technological University
1400 Townsend Drive
Houghton, MI 49931

Table of Contents

List of Graphical Materials

Abstract

The project, "Calibration of Seismic Attributes for Reservoir Calibration," has completed the initially scheduled third year of the contract, and is beginning a fourth year at no additional cost, designed to expand upon the tech transfer aspects of the project. From the Stratton data set we have demonstrated that an apparent correlation between attributes derived along 'phantom' horizons are artifacts of isopach changes; only if the interpreter understands that the interpretation is based on this correlation with bed thickening or thinning, can reliable interpretations of channel horizons and facies be made. From the Boonsville data set we developed techniques to use conventional seismic attributes, including seismic facies generated under various neural network procedures, to subdivide regional facies determined from logs into productive and non-productive subfacies, and we developed a method involving cross-correlation of seismic waveforms to provide a reliable map of the various facies present in the area. The Teal South data set has provided a surprising set of data, leading us to develop a pressure-dependent velocity relationship and to conclude that nearby reservoirs are undergoing a pressure drop in response to the production of the main reservoir, implying that oil is being lost through their spill points, never to be produced. The Wamsutter data set led to the use of unconventional attributes including lateral incoherence and horizon-dependent impedance variations to indicate regions of former sand bars and current high pressure, respectively, and to evaluation of various upscaling routines.

Our work on these four data sets is now essentially complete, and our attention is focussed on new tech transfer methodologies, including the use of tutorials and other examples on CD-rom as well as conventional publications and presentations. The results of the Teal South data set have already attracted some attention due to their implications for reservoir management and exploitation techniques.

Executive Summary

The project, "Calibration of Seismic Attributes for Reservoir Calibration," has completed the initially scheduled third year of the contract, and is beginning a fourth year at no additional cost, designed to expand upon the tech transfer aspects of the project. We have completed all essential work on four major data sets and have made intriguing conclusions in all of them. As the preparation of tech transfer items continues, we expect to find minor additional tasks to perform on some of the individual data sets, for completeness or demonstration purposes.

Our description of the work performed will follow each data set, and the discoveries made associated with them. A summary will present those same discoveries in terms of their relationship to the current state of the art in seismic calibration interpretation.

The Stratton data set has provided a challenge in thin-bed reservoir characterization in the absence of sonic-log calibration data. In general, the seismic character of potential productive zones is obscure in this data set, and horizons containing the pay zones are typically discontinuous. Previous work by other authors has demonstrated the apparent usefulness of simple attributes mapped along 'phantom' horizons which were tied at one well through a VSP and controlled by a constant offset from a nearby continuously tracked horizon. We have demonstrated in this project that this apparent correlation is an artifact of isopach changes, which dominate the interpretations based on simple attributes and on seismic facies analysis. However, if the interpreter understands that the interpretation is based on this correlation with bed thickening or thinning, reliable interpretations of channel horizons and facies can be made.

The Boonsville data set has provided another challenge in thin-bed reservoir characterization, in which the seismic character of a productive sand zone appears, indistinguishable from the character of a non-productive limestone to most commonly used attributes. In this case, the interplay of impedance and thickness conspire with tuning to produce the similarity in most attributes. This problem was attacked with two methods. In the first method, a technique was developed that made use of the well-log interpretations to divide the area into a number of facies, following a reasonable geological model; then the seismic attributes, including seismic facies generated under various neural network procedures, were used to further subdivide those regional facies into productive and non-productive subfacies. In the other method, a new technique involving cross-correlation of seismic waveforms was developed to provide a reliable map of various facies present in the area; we think this technique holds great promise for other data sets as well, and it appears to be extremely robust.

The Teal South data set has provided a surprising set of data, extremely rich in interpretation possibilities. We used the limited log data and excellent seismic data of this class III AVO bright spot reservoir in the Gulf of Mexico to develop a robust seismic petrophysics model through waveform (stratigraphic) inversion for acoustic impedance. We then used this model, together with a pressure-dependent elastic modulus relationship developed by us, to predict the future seismic response of the reservoir, as it was produced. Our predictions met the observations with uncanny accuracy. But observations of nearby, unproduced reservoirs also indicated a similar response, one that was not predicted with classical reservoir models or simulations. We concluded that these nearby reservoirs are undergoing a pressure drop in response to the production of the main reservoir, and that oil is being lost through their spill points (as gas comes out of solution), never to be produced. This set of observations may have serious ramifications for engineering and exploitation techniques throughout the Gulf of Mexico.

The Wamsutter data set provided our most-challenging opportunities. This thin bedded low-porosity sand within the Almond formation of the western US has demonstrated to other studies that conventional seismic attributes are not typically useful in identifying depositional facies or productive zones. We sought unconventional attributes that were designed to identify those features which we concluded should be in the seismic data as a result of knowing the rock physics associated with production. We found that a measure of lateral incoherence, developed by us, and applied along a phantom horizon designed to track a sand bar and its distal marine equivalent, provided extraordinary correlation with productivity from that sand bar. We also found that a technique we developed to identify high pressure from impedance variations along layers correlates strongly with results from the DFM technique of TransSeismic International and with zones of high production not associated with the sand bar; our interpretation is that these techniques are indicating zones of high fluid pressure and/or microfracturing. We also tested a variety of techniques of upscaling sonic and density logs to the seismic scale using the thin-layer effective medium model of G. Backus, and have significantly improved the tie between synthetic seismograms and real seismic data in this data set.

The main results of the project can be classified along these lines:

- Pitfalls (how to use 'phantom' horizons carefully)
- Unconventional attributes
  - Lateral extent of incoherence
  - Cross-correlation with 'type' seismograms
  - Impedance variation within specific layers
- Upscaling from sonic to seismic
  - Methodology
  - Recommendations for routine implementation (under development)
- Pressure-dependence of elastic properties
  - New relations based on (existing, from Han) dry-frame laboratory measurements
  - Importance of inclusion in time-lapse studies
- Reservoir behavior detected from time-lapse seismic observations

Our work on these four data sets is now essentially complete, and our attention is focussed on new tech transfer methodologies, including the use of tutorials and other examples on CD-rom as well as the conventional publications and presentations. The results of the Teal South data set have already attracted some attention due to their implications for reservoir management and exploitation techniques.

Introduction

The objectives of this project are three-fold: To determine the physical relationships between seismic attributes and reservoir properties in specific field studies; to improve the usefulness of seismic data by strengthening the physical basis of the use of attributes; and, in the third year of the project, to test the approaches suggested or developed during the first two years on at least one new data set. In association with these studies, collaboration with corporate partners and technology transfer as ideas are developed and tested are ongoing integral components. We have extended the project to a fourth year (at no additional cost) to implement new technology transfer components, including tutorials and other approaches.

This report will summarize the current state of the various tasks of the project, following the Project Work Plan. Then it describes the results of our analyses of each data set in some detail. Finally, it summarizes the results and conclusions.

Task 1: Project Management

Project management encompasses reporting and project support. Reporting is on schedule. Project support is on schedule after some initial redirection of efforts during the first year (resolved by the hiring of additional support personnel in systems administration).

Training for some of the software packages has been accomplished by attending training courses conducted by the companies providing the software. To date, we have had members of our team take part in training on the following packages:

- GeoQuest GeoFrame products
- IC2 from Scott Pickford
- Stratimagic from Paradigm Geophysical
- Jason GeoScience

We also use Landmark Graphics products, GXTechnology products, and Seismic Micro-Technology products.

Task 2: Borehole Data

Borehole data for this project consists of three types: existing log data, existing core data, and new core data. We have made use of all existing data, and have obtained new information on well-completion histories in Stratton field for help in identifying productive intervals in this complex field. We made new measurements on existing core from the Wamsutter area to help in characterizing the thin-bed nature of the formation. And we have made novel use of inverted seismic data to constrain rock properties where log data was incomplete.

The Borehole Data task portion of this project is complete.

Task 3: Processing

We have conducted most of the processing of data that is required at MTU using software provided by donors; additional processing (for the DFM) has been conducted by a subcontractor.

To date, our processing efforts have included the following:

- prestack processing of multiple 2D lines to evaluate acquisition artifacts,
- poststack processing for attribute extraction,
- poststack processing for variance/coherence,
- poststack inversion for acoustic impedance, and
- synthetic seismogram generation.

New routines have been written using MatLab or other languages appropriate to the task. No significant additional processing is anticipated in this project, other than what may be required to support the technology transfer component.

Task 4: Visualization

In our project organization, visualization includes the massive effort of data management as well as the specific techniques for visualization. We have been able to utilize the 3D visualization capabilities of our software packages for interpretation of the data we have processed, and have put the processed (DFM) data volumes from a subcontractor (TransSeismic International) into a 3D visualization package for easier interpretation.

The software that we are using provides outstanding visualization capabilities, and we continue to develop approaches to viewing the data in ways (including animations and illuminations) that make interpretation and transfer of ideas straightforward. We continue to find new ways to visualize the results of our work, and anticipate some additional effort in this area to support the technology transfer component.

Technology Transfer

Our web site is complete and is updated regularly (http://www.geo.mtu.edu/spot). We presented an oral presentation and posters at the annual AAPG meeting in Denver, CO in 2001, oral presentations at the SEG meeting in Calgary in 2000, published an invited review paper on "Reservoir Geophysics" in GEOPHYSICS, 2001, and have a manuscript in press in THE LEADING EDGE for October, 2001. We are working on at least four other publications and on novel techniques for providing experiences in seismic calibration for interpreters.

Results and Discussion

This section of the annual report first describes current results for each data set, then discusses these results and suggested interpretation as a whole.

Stratton Field, South Texas

The public-domain data set from Stratton field has provided the challenge of imaging features below seismic resolution, in an effort to identify the channels known to be present in the volume. Some of the channels are readily seen, particularly at shallow levels, but most channels can only be inferred by correlation with well data and through recognition of subtle features on the seismic data.

The Stratton field produces from the Frio formation from reservoirs contained within a series of meandering channel-fill deposits. The Texas Bureau of Economic Geology (BEG), in a project supported by the U. S. Dept. of Energy (DOE) and the Gas Research Institute, studied this field in some detail (e.g., Hardage et al., 1994), in an effort to use seismic data to aid in identifying sources of reservoir compartmentalization. They also made a subset of the data available for public use. In their study, the BEG found that seismic data could resolve very small channels at considerable depth: down to 10 ft (3 m) thick, 200 ft (61 m) wide, at depths greater than 6000 ft (1800 m). They interpreted some channels in the time structures (assuming that they represent paleo-topographic surfaces along which the streams flowed). They were generally unable to 'track' the specific horizon of interest in this thin-bedded environment, partly because not all horizons were continuous, and partly because the geologic bed of interest (as indicated in well logs) did not correspond to a clear peak or trough. They made extensive use of 'phantom' horizons (our word, not theirs, but now in common usage), at a constant offset from readily-tracked horizons, and tied at one well where a VSP was conducted.

We have extended an approach used by the BEG to include a complete wave-shape matching routine rather than a simple point attribute at the VSP-controlled time of the reservoir bed. The BEG approach is straightforward and readily accomplished on most workstation software packages. The approach we are using has only recently become available. The technique we have applied is implemented in the commercially available package Stratimagic, which uses a neural-network method to divide the wave shapes found in the interval being considered into a (user-specified) number of different 'facies.' The maps displaying the spatial locations of the different facies can often provide a picture of geologically meaningful features, such as channels or crevasse-splays. We pursued this approach because the BEG result indicates that subtle differences in wave character provide strong clues to the location of channels or to the compartmentalization of the reservoirs.

Our observations and maps initially were similar to those obtained by the earlier studies conducted by the BEG. However, our interpretation of the physical origin of the features on these maps is significantly different from theirs. We have concluded that most of the features recognized from these phantom horizons are in fact due to isopach differences between the phantom horizon and the local horizon; these may, in turn, be due to the presence of channels (in one case this is clear). But the attributes themselves are not directly associated with lateral changes in horizon properties – instead, the 'phantom' horizon crosses true horizons as the interbed thickness varies, and the determined attributes naturally change as these beds are crossed. The details are presented in the following summary.

BACKGROUND

The Stratton field is located in South Texas approximately 30 miles southwest of Corpus Christi (Figure 1) in Kleberg and Nueces counties. The 2 square-mile migrated 3-D seismic volume, containing 100 inlines and 200 crosslines spaced at 55 feet intervals, sampled at 2 ms in time, has been provided by the Texas Bureau of Economic Geology (Hardage et al, 1994) together with data from 21 well logs and one Vertical Seismic Profile (VSP). The data were acquired using an 8-120 Hz Vibroseis sweep. Like many gas fields with a long production history, the log suites vary greatly among the wells. The wells were drilled from the 1950's to the early 1990's and generally were logged with gamma, resistivity, and neutron logs. Since sonic logs are not available for any wells in the field, we rely on a checkshot derived from the VSP. There are no log data available for the nonproducing shallow channel region investigated here. We have received limited production data provided by the operator Collins & Ware.

The major producing formations are the nonmarine fluvial Upper Vicksburg and Middle Frio formations (Figure 2). The Upper and Middle Frio contain nonmarine channels; the Lower Frio has been described as a coastal plain, and the Upper Vicksburg Formation is thought to be deltaic in origin. The Frio formation is comprised of thin-bedded sandstones and mudstones as thin as 10 ft. A series of growth faults in the Vicksburg terminate at an unconformity at the base of the Frio. The horizons and growth faults are identified on a seismic section in Figure 3.

In this study, we analyzed a shallow non-productive horizon containing an apparent channel, and a deeper productive horizon just above the Frio-Vicksburg unconformity.

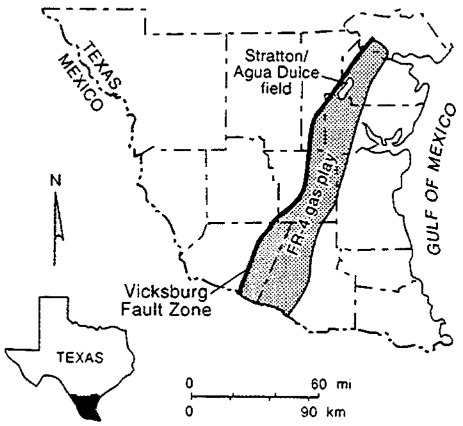

Figure 1 Location of the Stratton Field (adapted from Hardage 1995).

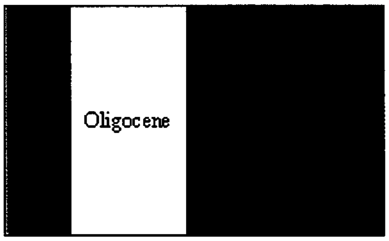

Figure 2 Stratigraphic sequence of the Oligocene

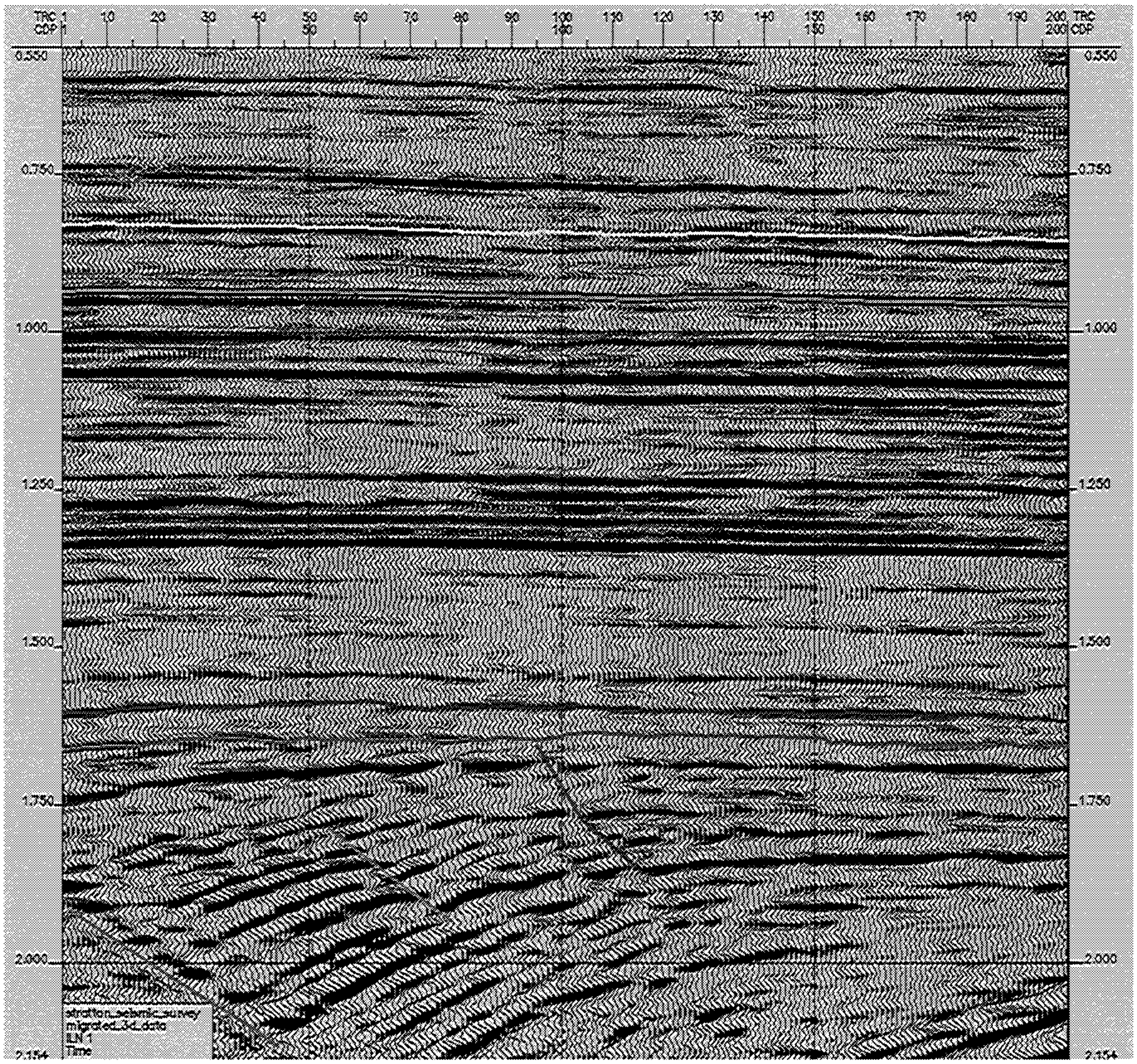

Figure 3 Seismic section showing the two horizons studied: a channel region at approximately 842 ms and the primary producing region at approximately 1640 ms in time. The heavily faulted area is due to a series of growth faults in the Vicksburg formation.

PHANTOM HORIZON TECHNIQUE

Many of the horizons of the Stratton Field were difficult to track across the entire survey. To address this problem, we followed a suggested procedure outlined by Hardage et al (1994) adapted to modern workstations. A shallow channel region and a deeper producing region were chosen as test cases (identified on Figure 3). A reference horizon was chosen close to each horizon of interest and tracked throughout the survey. Using the VSP data provided, each horizon was associated with a specific depth and the time differences between the horizons noted at that well. Using this fixed time difference between each reference horizon and its associated target depth/time, a new 'phantom' horizon is created. [This process is equivalent to flattening on a horizon and selecting a time slice relative to it.]

Conventional attributes

To better image the shallow channel and deeper producing horizons, conventional attributes were derived. Conventional attributes can be divided into point based and interval based attributes. Point based attributes include, but are not limited to, amplitude, instantaneous amplitude, instantaneous phase, and instantaneous frequency. These attributes are derived directly on a horizon. Interval attributes involve using a time window based upon an interval of a horizon or an interval between a horizon. Calculations that involve averages over a given time window, such as RMS amplitude, are examples of interval based attributes.

Facies classification technique

The term "seismic facies classification" can have many different meanings. For the purposes of this study, seismic facies classification is used to describe the process of grouping the traces of a survey into a limited number of categories based on the shape of each trace over a fixed time window (Poupon et al, 1999). To perform a seismic facies classification, a horizon and a fixed time window surrounding the horizon of interest should be chosen and the amplitudes extracted with the associated times. For example, if a 12 ms interval is chosen, with a 2 ms sample rate, there will be 7 amplitude values at 0,2,4,6,8,10 and 12 ms in time within the window. These samples are used to compute gradients by calculating the change of the value between samples (Figure 4). For this example, a list of 6 gradient values would be created. The series is then normalized by dividing each value by the largest gradient value. The series can be thought of as a 6 dimensional vector with each dimension having a value ranging between minus one and one. These vectors are then obtained for every trace in the survey or area of interest. Next, a neural network process searches for clusters of these vectors, a process roughly equivalent to finding clusters of waveshapes. Each trace is then placed into a category or class, based on these clusters. Each trace has been classified based on its normalized gradient vector, and it is primarily the trace shape (changes in amplitude) that drives the classification rather than direct amplitude values. The number of classifications will determine the resolution of the trace shape analysis. As more classes are used, smaller and smaller details will become visible in the analysis, which are shown as color changes in a facies classification map, but the noise in the image will also tend to increase. If more detail is needed, the survey can be subdivided into multiple regions to improve the classification process. A smaller region will have fewer traces and will need fewer classifications to provide the same amount of information.

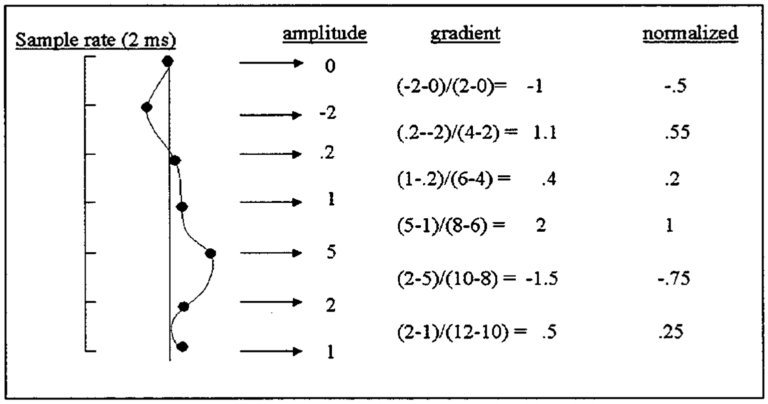

amplitude	gradient	normalized
0		
	(-2-0)/(2-0)= -1	-.5
-2		
	(.2--2)/(4-2) = 1.1	.55
.2		
	(1-.2)/(6-4) = .4	.2
1		
	(5-1)/(8-6) = 2	1
5		
	(2-5)/(10-8) = -1.5	-.75
2		
	(2-1)/(12-10) = .5	.25
1		

Figure 4: Calculating normalized trace gradients for the facies classification.

The previous work performed by Hardage et al (1994) limited the analysis to point based amplitude observations. If a point based amplitude analysis can give information about a feature, then performing an analysis using the entire trace over a window of time can be expected to provide more details about that feature. Furthermore, if a single instance of time near a horizon can give useful information, using a window of time above and below that horizon should be able to give even more information. For example, if the producing region is present either slightly above or below a horizon, utilizing a time window that includes these areas may show features that might have been missed if the attributes were calculated directly on a horizon. Examining the trace shape over the time window could provide clues to the inherent waveshape property or properties that are associated with the fluid content. Using neural network technology, the traces (over a certain window of time) can quickly be divided and placed into a similar model trace, which can then be used to identify structural features. Classifying the shape of the trace should allow the delineation of more detailed features over a region than using a single point based attribute. The more classes used, the fewer the number of traces in each class, and the more detailed the analysis.

For the first example in the Stratton Field, a channel will be identified, and the facies classification technique will be used to later separate the traces based upon differences within the trace.

SHALLOW CHANNEL REGION

An apparent channel at approximately 842ms can be located in the shallow region of the Stratton Field. This channel is easily identified from amplitude measurements on a time slice (Figure 5), but a phase change is introduced across this time slice by the gentle dip of the beds.

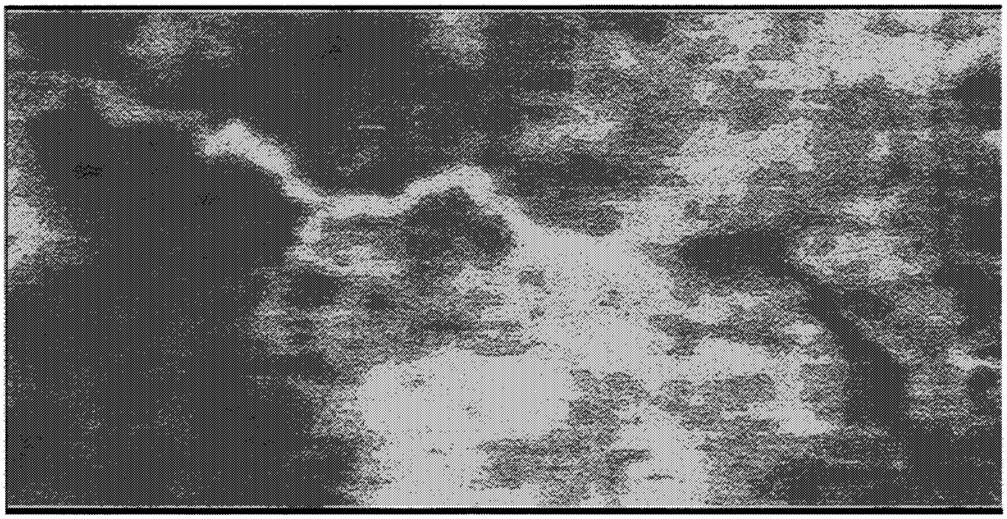

Figure 5: The shallow channel region at approximately 842 ms in time. A phase change occurs (from light to dark gray) across the image due to the gentle dip of the horizon.

Conventional Attributes on the shallow horizon

Figure 6 shows the time structure of the interpreted horizon containing the shallow channel. Although visible, the channel is not clearly represented on this structural time surface, because the channel is consistently about 2 ms later than neighboring traces on the horizon, yet the horizon exhibits total relief (due to gentle dip) of about 40 ms obscuring the small time differences. Because the channel differs from the surrounding traces by only 2 ms, the effect of the dip must be removed to emphasize these differences. A number of additional attributes were extracted along this horizon, none of which provided a more clear indication of the channel than the time structure.

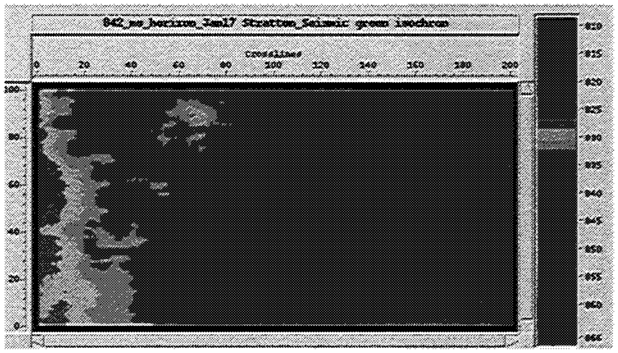

Figure 6: Structural (time) surface of the picked horizon outlining the channel.

Conventional attributes using a phantom horizon

A continuous horizon (found at 945 ms at well 9) was chosen and named reference horizon A (Figure 7). The time difference between the interpreted shallow channel horizon and reference horizon A at well 9 is 101ms. The time difference was chosen to overly the non-channel facies over most of the survey area. The new phantom horizon was created with the intention of removing the general dip structure from the shallower horizon. Attributes were then calculated over this phantom horizon, some of which are shown in Figure 8. Both the amplitude slice and RMS amplitude (which was calculated over a 20 ms window of time centered on the phantom horizon) do an excellent job of defining the channel, largely because the phantom horizon gently accounts for the dip, while cutting across the channel feature.

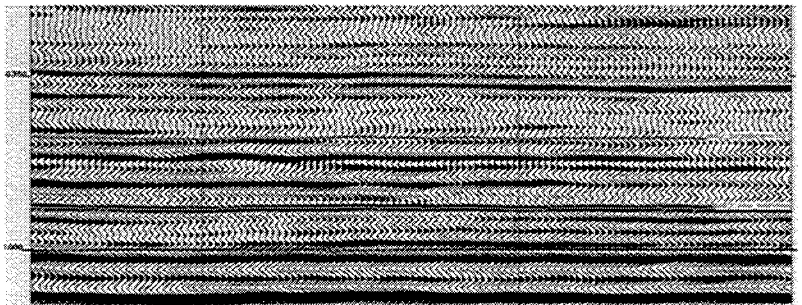

Figure 7: The phantom horizon created by subtracting 101 ms from reference horizon A.

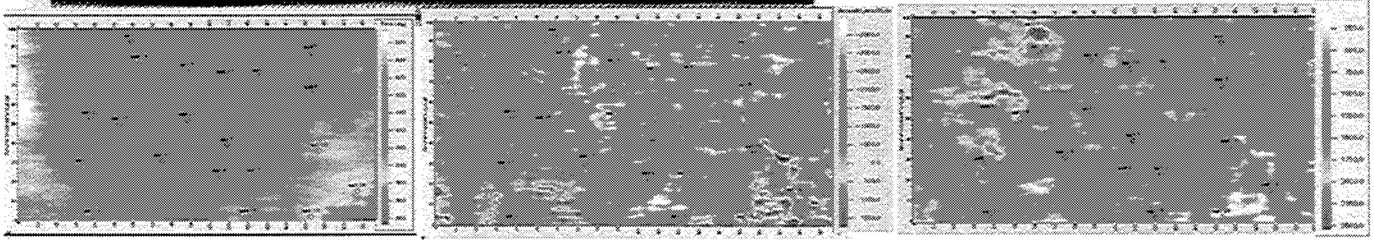

Left side: Time. Center: Amplitude. Right: RMS Amplitude

Figure 8: Attributes of the phantom horizon corresponding to the shallow channel.

Facies Classification of shallow channel region

The final approach applied to the channel horizon makes use of the facies classification technique. A 20ms time window centered on the phantom horizon was chosen to perform the trace shape analysis. An unsupervised neural network with 14 classifications produced the image shown in Figure 9a.

The relatively clear boundaries emphasize the sinuous form of the channel. Figure 9b shows the model traces used to create the classification. Notice that a gradual time shift of the wavelets has occurred with approximately a 1 ms shift from one classification to the next. The channel is represented by the 13th and 14th classifications shown as dark blue and purple colors on the facies map. In effect, the trace shape of the channel has been classified by a small time delay; the facies classification technique is highly sensitive to time shifts.

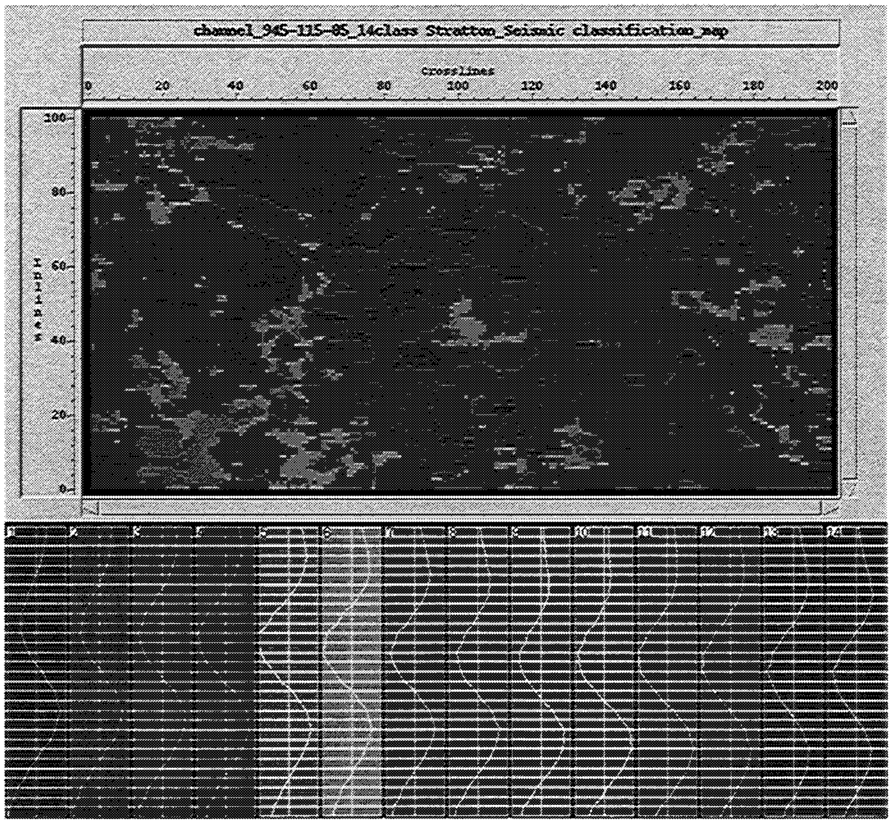

Figure 9: Unsupervised facies classification of the shallow channel region.

9a (upper figure) shows the classification, and figure 9b (lower) shows the wavelets used in the classification.

Discussion of the shallow channel region

In the shallow region, both point-based amplitude attributes and the interval attributes were not effective in imaging the channel when performed directly on the tracked horizon. The phantom horizon permitted much better identification of the channel than the original horizon, primarily due to the time shift involved. That is, because the channel reflection arrives about 2 ms later than the surrounding non-channel horizon, the phantom horizon encounters a slightly different phase at the location of the channel, and its amplitudes are correspondingly affected. The difference results in the dramatic color contrast between the feature and the surrounding survey. It is this color change that allows the viewer to separate the channel from its surroundings.

The seismic facies classification technique based on trace shape works for similar reasons. Each trace is classified as a multidimensional vector, with time shifts having a large impact upon the classification. The small time shift results in model traces created by the neural network that specifically image the channel. To image structures with small time changes, both phantom horizons and facies classification techniques based on trace shapes can be effective, but the user should recognize that the classification based on a phantom horizon may simply be due to isopach differences between the features being identified and the reference horizon.

THE REGION OF GAS PRODUCTION

For the second portion of the study of the Stratton field, we attempted to image a much more subtle case in the deeper region of production. Assorted well logs and limited production information are available for this region.

In the Stratton field, the F39 horizon is one of the primary producing intervals and appears on the seismic data at approximately 1640 ms in time. Unlike the channel horizon (tracked on minimum amplitude or trough), the F39 horizon was tracked using a maximum (peak) determined from times provided in Hardage et al (1994) at each of the well locations. Figure 10 shows the time structure of this horizon; we see a gently arching structure across the survey. As in the previous examples of the shallow region, amplitude, RMS amplitude, and instantaneous frequency were unable to decisively identify any channel or potentially productive zones. A phantom horizon was therefore created to better image this region.

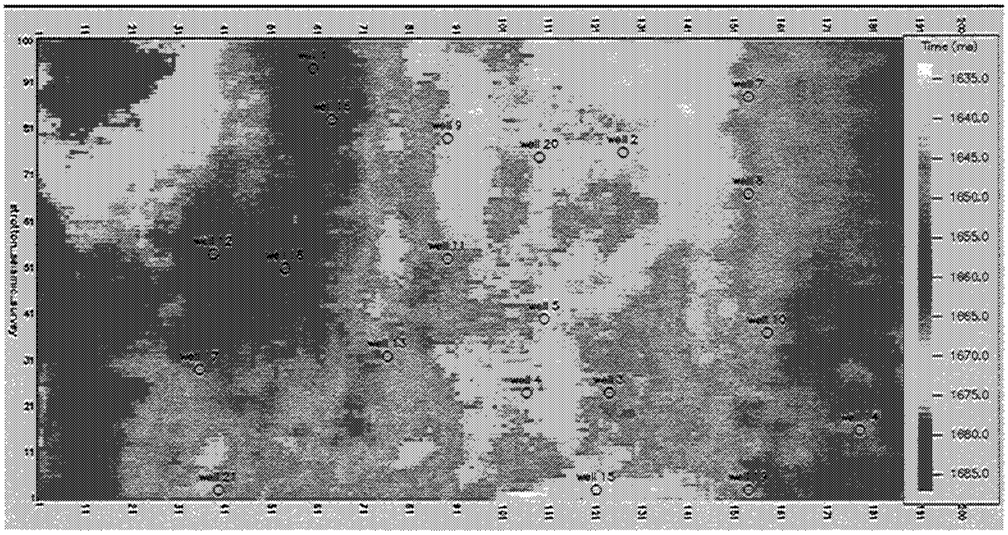

Figure 10: Time structure on the F39 horizon.

Conventional attributes using a phantom horizon

The F39 horizon was difficult to track due to tuning effects. The phantom horizon technique used by Hardage et al (1994) was reproduced here: the F11 horizon was tracked and a phantom horizon was created at the level of the F39 horizon at the VSP well (59 ms later; see Figure 3, presented earlier). We then calculated attributes over this phantom horizon. Figure 11 shows the amplitude and RMS amplitude calculated on this phantom horizon. Examining these attributes show strong north-south linear features, and one may be tempted to conclude that these represent stratigraphic differences in the F39 horizon.

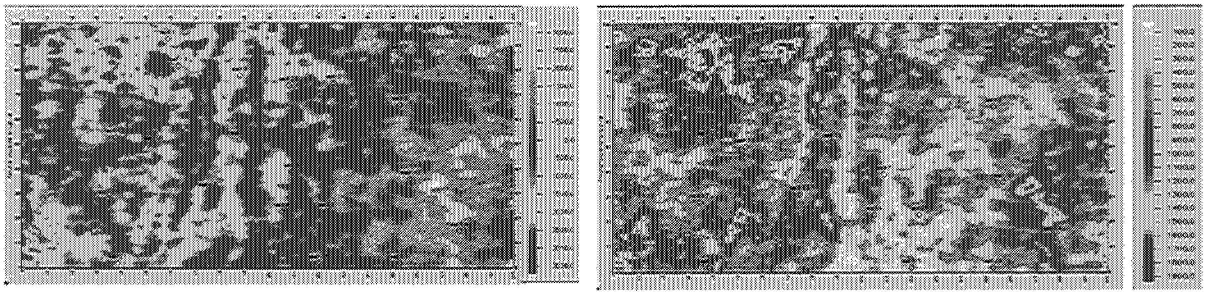

Left: Amplitude *Right: RMS Amplitude*

Figure 11: Attributes on the phantom horizon corresponding to the F39 level.

Facies classification of the deeper producing region

Using the Facies classification technique on the phantom horizon and a 25ms time window (20 ms above and 5 ms below), we see a dramatic time shift in the classifications (Figure 12). Investigating these features more closely yields surprising results. These linear features are not channel regions or areas of faulting as might be expected; they are areas (see Figure 13) where the true relief of the F39 horizon is much greater than that of the phantom horizon. The linear features are caused by the phantom horizon passing through alternating peaks and troughs.

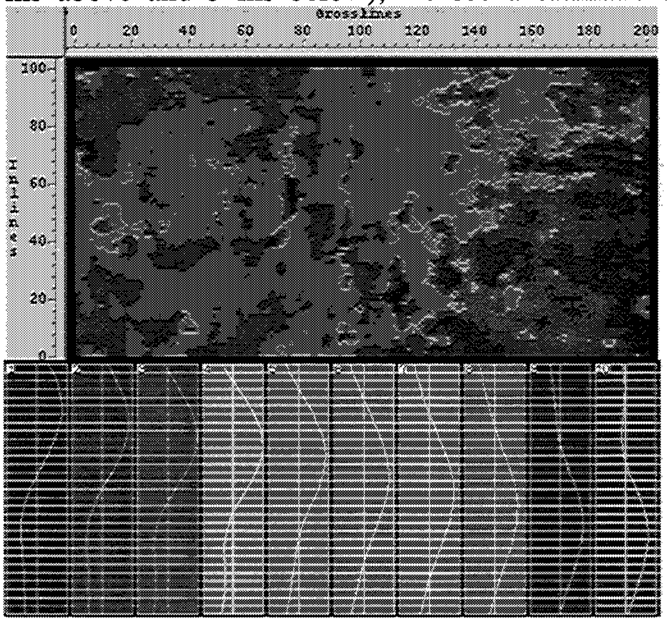

Figure 12: Seismic facies classification of the F39 Phantom horizon.

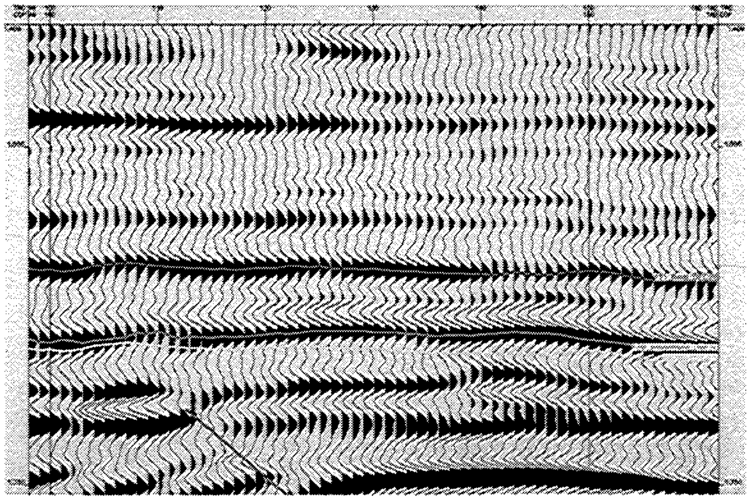

Figure 13: Horizons associated with tracking F39.

<u>Red</u> Horizon: F11, used for reference

<u>Green</u> Horizon: Tracked F39 horizon

<u>Yellow</u> Horizon: Phantom F39 horizon, based on the F11 reference

To better portray the area between the F11 and tracked F39 horizons, an isopach map was created. Figure 14 shows that the isopach thickens to the west from 29 ms to 66 ms in time. These two horizons are not conformable and do not have the same dip; therefore, a phantom horizon based on a constant time difference is not advisable.

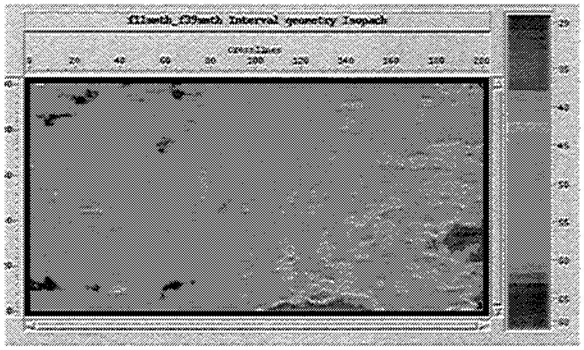

Figure 14: Isopach of time separation between the F11 horizon and the tracked F39 horizon.

DISCUSSION

To deal with the difficulties posed by non-conformable and/or dipping beds, we offer two suggestions. First, choose a reference horizon that is highly conformable to the horizon of interest. Most often this will be a horizon that is closely adjacent to the interpreted horizon. An isopach map showing the time differences between the reference horizon and the poorly tracked horizon of interest will aid in determining the degree to which the two horizons are conformable. In some cases, as in the F39 horizon, there are no nearby conformable horizons. Therefore, attributes must be calculated directly from the poorly-tracked horizon. We suggest using a waveshape-based facies classification scheme. As with the channel horizon, the gradually increasing time separation of the peaks is the driving force behind the classification. The trace shape analysis is very sensitive to time shifts caused by thickening or thinning of the nearby horizons. In the case of the deeper producing region, even anchoring on the horizon to be classified, resulted in a classification based on stratigraphic thickening.

Our second suggestion is to create proportional slices between the two horizons. This would work best for regions that do not have nearby conformable reference horizons. Two horizons, bracketing the poorly-tracked horizon of interest, can be used to create a set of proportionally interpolated horizons, which can be used, as phantom horizons that may be fairly conformable to the intermediate beds. These proportional slices will be less affected by conformable horizons since the medial slices will be used. Measuring amplitudes over these proportional slices may provide an alternative approach to horizon slicing.

CONCLUSIONS (STRATTON FIELD)

The use of phantom horizons can provide strong assistance to the geophysical interpreter, particularly in areas where the level of interest does not correspond directly to a trackable event. The use of seismic facies classification schemes can provide additional strong assistance. But both approaches depend strongly on the phantom horizon's conformability with the horizon of interest. If the events are not conformable, attributes extracted along the phantom horizon will correlate more strongly with isopach differences than with true formation properties within a specific layer. On the other hand, if the interpreter recognizes these attributes as such, the phantom layer and its attributes can serve as a proxies for those geologic features that cause the thickening or thinning, but it is essential that the interpreter recognize them as such.

Boonsville Field 1: Quantitative seismic facies analysis for thin-bed reservoirs

In this section, we describe a new pattern recognition model developed to recognize the subtle geological and geophysical features of a thin-bed sequence and predict thin-bed reservoirs, based on cross-correlation of seismic traces with one or more traces believed to represent specific depositional environments. Our approach has the following characteristics: (1) It corrects for the possible mistracking of top horizons by searching about a time window specified by the user; (2) It presents seismic facies as continuous values by introducing the modified cross-correlation algorithm, as opposed to a limited number of clusters; (3) It more easily performs one or more supervised trace pattern recognition and combines each of them into a seismic facies.

INTRODUCTION

Using 3-D seismic data integrated with well data to build reservoir depositional model is routine work and seismic stratigraphy plays a significant role, albeit in a qualitative fashion. However, it is not uncommon for thin sequences to exhibit seismic trace pattern changes that are subtle and with ill-defined termination patterns. Our case study area poses an additional challenge: how to distinguish thin-bed reservoirs and thin-bed non-reservoirs when they appear similar at seismic scale. It is this second challenge that we address in this section.

The average acoustic impedances of the shale, sandstone, and limestone of the Boonsville Field are 30000, 36000 and 40000 ft/s*g/cc respectively (Figure 15), indicating that we could separate the sandstone reservoirs from the limestone non-reservoirs if we were capable of identifying their acoustic impedance with any confidence. However, the discrimination is very difficult in this field because the limestone and sandstone layers appear similar at the seismic scale.

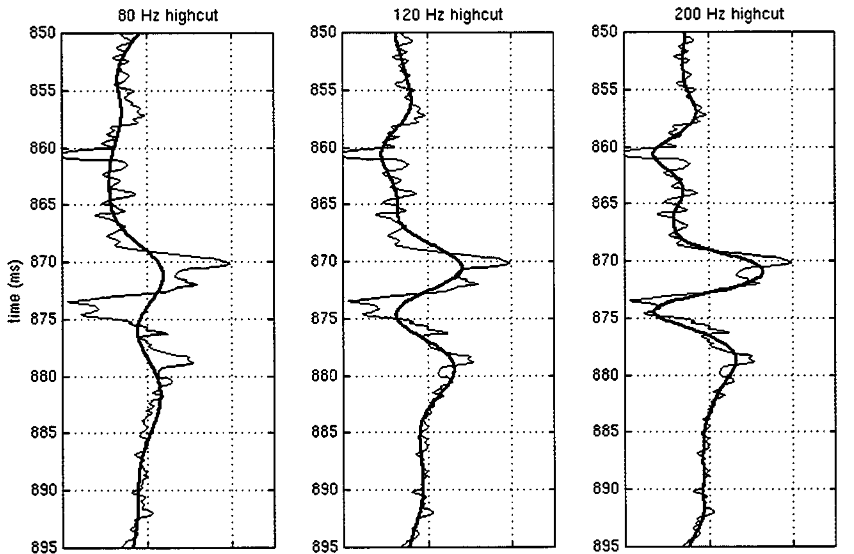

Figure 15: Sample impedance contrasts in Boonsville field.

The fast bed at about 870 ms two-way time is limestone, and the fast bed at 878 ms is a sandstone; the other formations are mostly shales. The original impedance is shown in blue on all traces, and the filtered impedance is shown in red, using a high-cut filter as labeled. Notice that below 120 Hz, the distinction between the limestone and sandstone beds is insignificant.

A sonic well log has a resolution less than 5 feet in comparison with seismic resolution, up to 50 feet for the Boonsville data set. The frequency bandwidth of the Boonsville 3-D seismic data is from 15 to 120 Hz while the frequency bandwidth of the velocity log ranges from 0 to greater than 500 Hz. High-cut filtering is required to "upscale" the frequency bandwidth of the well data to the seismic data. As a result of high-cut filtering, the high impedances of the thin-beds are averaged with nearby lower impedances. The final effect is that the higher impedance of the limestone non-reservoir appears to be close to the impedance of the sandstone reservoir. A more complete treatment of the problem would include Backus (1962) averaging of the thin beds, with details depending on the frequency content of the wavelet, but the net effect will still be the overall reduction of the highest impedance resolved. [This approach is considered later in this report, with the Wamsutter data set.] Therefore, two rock types may easily appear similar at seismic scale and become difficult to distinguish through the interpretation of a seismic data set alone, even though the actual thin-bed impedances are significantly different

Our study area is the Boonsville Field of the Fort Worth Basin in north central Texas (Figure 16a). The data set includes 5.5 square miles of 3-D seismic data set and 38 wells with modern logs , made available through the Texas Bureau of Economic Geology (Hardage et al., 1996a). Here we concerned ourselves within the Caddo sequence of the Pennsylvanian Group (Figure 16) although other productive sequences also exit in the area.

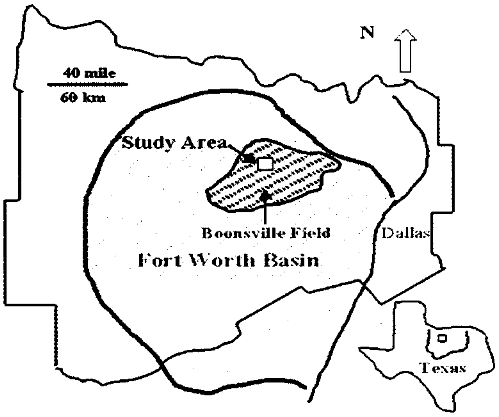

Figure 16a: Location map of the Boonsville study area.

Figure 16b. Traverse seismic line through the main delta showing the Caddo sequence.

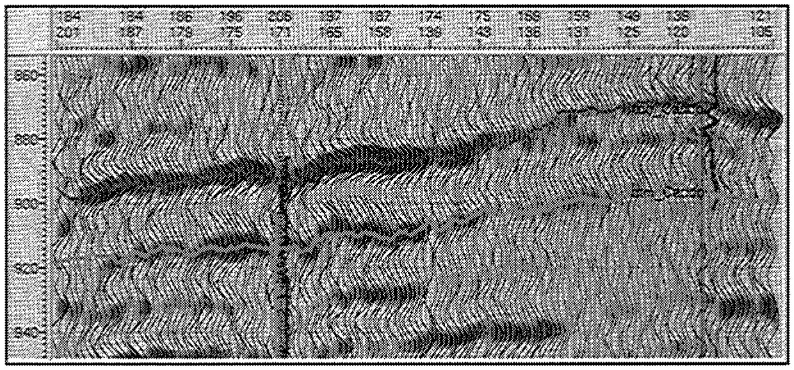

The reservoir characteristics and the related data set meet our basic requirements to ensure reaching the research goals. Some features of the targeted Caddo sequence are: hydrocarbons are produced from the thin-bed sandstone reservoirs with thicknesses totaling 0 to 52 net feet of the Caddo sequence, with a gross thickness of 80-150 feet; the tight limestones have known thicknesses of 0 to 30 feet and appear similar to the thin-bed sandstones at seismic scale; the depositional environment is dominated by a delta system; both the sandstone and limestone are embedded in the shale-rich sequence and characterized by higher P-wave velocities and higher densities, thus generating higher acoustic impedances; both the sandstones and limestones are highly variable laterally and vertically.

Our primary research goal is to establish a depositional model of the thin Caddo sequence using the 3-D seismic data integrated with well data. In this study, we first build a depositional model using the well data only, and then examine some existing approaches to the use of seismic data for facies analysis, such as trace coherence and classification. A new method will be presented to recognize the subtle geological and geophysical features of the Caddo sequence, based on cross-correlation of seismic traces with one or more traces believed to represent specific depositional environments.

WELL-BASED DEPOSITIONAL MODEL

The depositional system of the Pennsylvanian Atoka Group has been studied by Thompson (1982; 1988), Glover, (1982), and Lahti et al. (1982). However, these studies were mainly focused on the entire Fort Worth Basin. Hardage et al. (1996b; 1996c) and Carr et al. (1997) analyzed the reservoir distribution and depositional subfacies using a few typical wells from this study area, but their model is not sufficiently detailed to be useful for facies analysis of this thin Caddo sequence. In addition, the tight non-reservoirs were generally not studied even though both the limestones and reservoir sandstones exist and appear seismically similar in the Boonsville Field. Therefore, a depositional model was established with a concentration on reservoir distribution and the discrimination of the sandstone from the limestone. The techniques involved include well log trend recognition and lithology determination.

The well log trends and lithologies analysis are summarized in Figure 17 and the well log trends from representative wells are illustrated in Figure 18. The main delta system was recognized in the east and the possible second delta system was observed at the northwestern corner, but appears to be mostly outside of the study area (Figure 18). The main delta system was divided into three delta subfacies: distal channel in the east margin, proximal delta front in the east, distal delta extending to south and northeast, and interdelta in the south and southeast. As depicted in a cross-section through the main delta system (Figure 19), the depositional subfacies and reservoir distribution in the eastern oil producing region are characterized by the distal channel and the proximal delta front are the depositional subfacies in which the thickest sandstone reservoir (up to 52 ft) was deposited; the distribution of limestones is limited, but the limestones can be correlated as the GR log trend is similar and correlative; the sandstone reservoirs are widely distributed in the delta front subfacies.

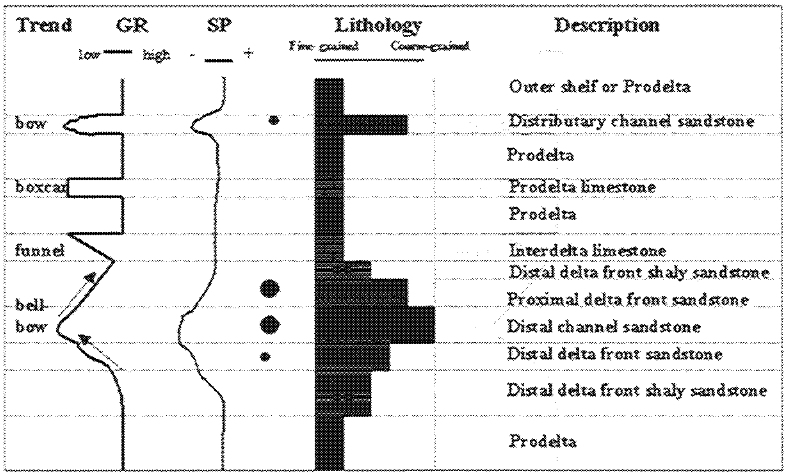

Figure 17: Generalized well log trends and corresponding depositional subfacies and lithologies of the Caddo sequence.

(Modified from Coleman et al., 1982; Thompson, 1982; Emery et al., 1996; Hardage et al., 1996b,; and Carr et al., 1997)

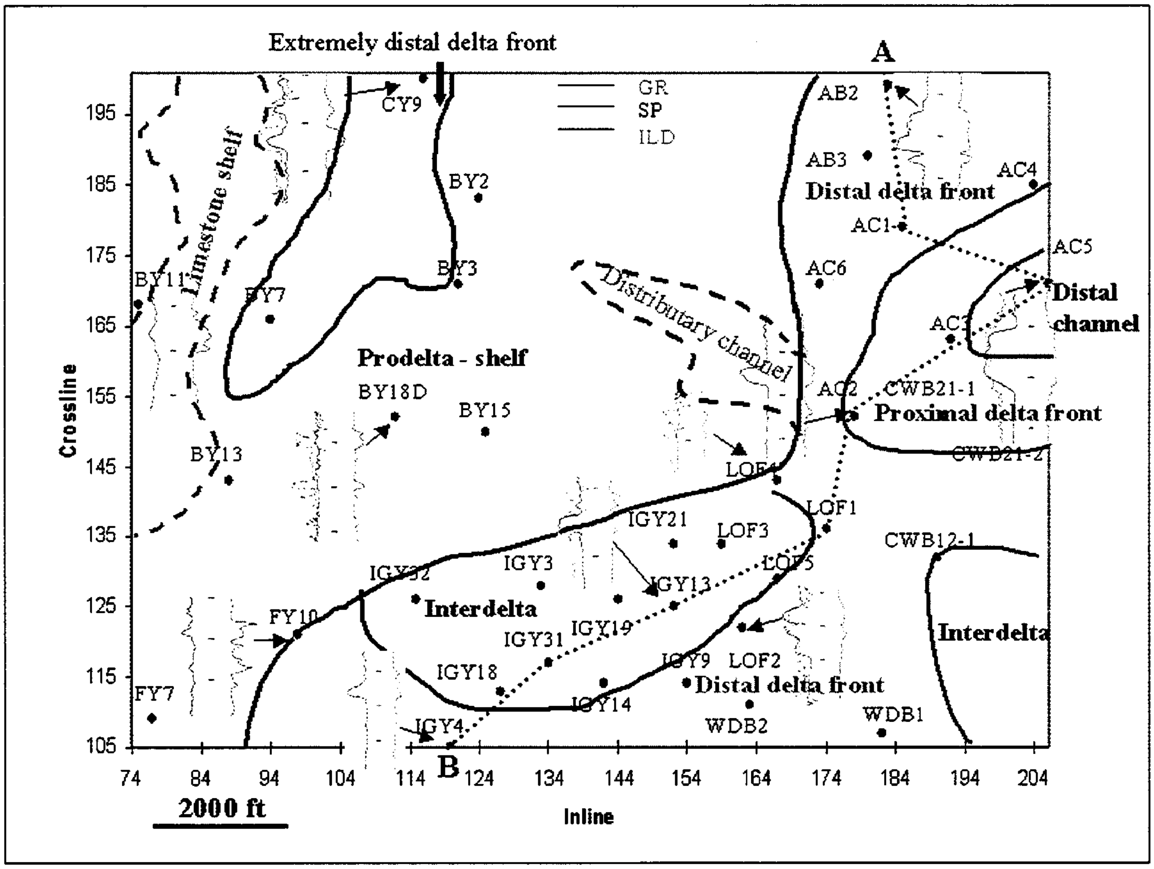

Figure 18: Representative well log trends and depositional subfacies of the Caddo sequence based on well data, with a possible limestone shelf and distributary channel based on seismic inversion. Cross-section A-B is indicated by the dashed line, and used in other figures.

The second delta system observed from the well data was detected at the northwestern corner. However, the main delta body remains outside the study area (Figure 18) and the relationship of this delta system (or sub-system) with the main delta system (or subsystem) in the east remains unclear.

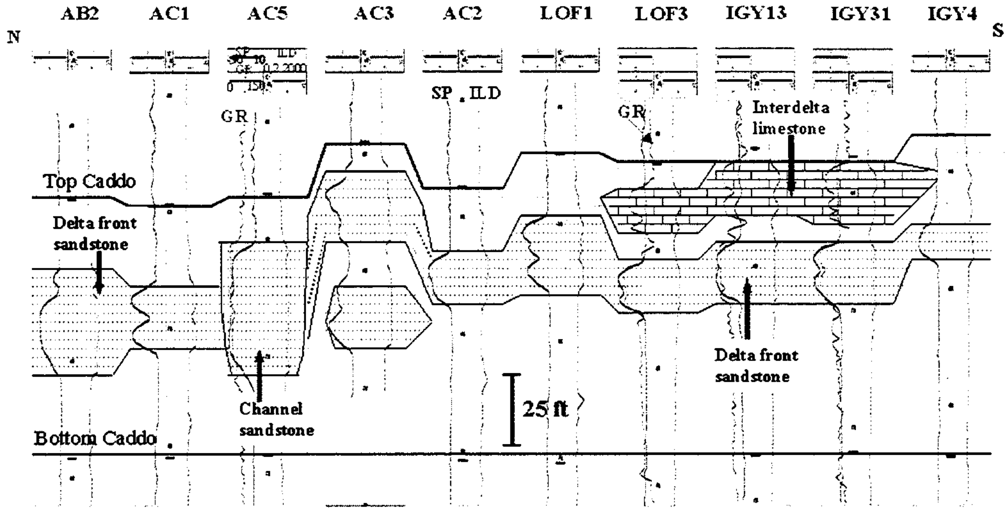

Figure 19: Well correlation and interpretation for depositional subfacies and lithology; the well section has been flattened on the Bottom Caddo marker.

The rest of the region is dominated by the prodelta or shelf, filled with shales and limestones. The SP log trend is a flat base line while the GR log pattern is a "boxcar". The "boxcar" indicates the prodelta limestone. No good reservoir sandstone was found in the prodelta subfacies, and instead, the shaly sandstones were recognized and no oil was produced from them. The maximum known thickness of the limestone in prodelta subfacies is 30 feet at well BY11 and BY13. However, the simulated acoustic impedance data reveals that a narrow north-south-oriented thicker limestone zone might exist in the west that will be discussed later.

SEISMIC TRACE PATTERN AND DEPOSITIONAL MODEL

Chen et al. (1997) suggested that more than 20 seismic attributes (not all of them are independent) would be useful in constructing reservoir depositional model. Other researchers (Horkowitz, et al., 1996; Hardage et al., 1996b; Cooke, et al., 1999) claimed that instantaneous frequency and/or instantaneous phase are effective at highlighting facies changes. Similarity analysis based on multiple point-based attributes, their means and deviations was used to map seismic facies (Michelena, et al., 1998). However, these point-based attributes only describe one aspect of a complicated seismic trace shape. The trace-based attributes may be a natural solution for better defining facies. In this study, two widely used approaches, coherence and trace pattern classification will be examined before a new technique is presented and tested.

Like the well-log trend, seismic trace pattern can be used to define a depositional facies. Notice that the patterns of the synthetic traces created from velocity and bulk density well logs do not perfectly match the real seismic traces because of different measurement scale, assumptions, and noise involved. However, they indicate that different depositional subfacies and reservoir distribution correspond to the changes in seismic trace patterns, which is the petrophysical basis for using seismic trace pattern to construct depositional subfacies.

SEISMIC TRACE COHERENCE

Seismic trace coherence is a measure of lateral changes in the seismic trace pattern and is based on a cross-correlation measurement. Bahorich et al. (1995) invented this technique and has since been modified by introducing semblance, structural dip and azimuth (Marfurt et al. 1998; 1999). Bahorich et al. (1995), Marfurt et al. (1998; 1999), Cooke (1999), and Chopra (2001) demonstrated that coherence can be used to define stratigraphic features. Our study suggested that the resolution depends upon the scale and the degree of variations in the patterns of neighboring traces. In particular, coherence may not be helpful if the changes in the patterns of neighboring traces are gradual, in which case, all of the coherence values are almost identical and no features are apparent. Furthermore, because the algorithm compares the neighboring traces along inline and crossline directions or traces in small regular-shaped (elliptical or rectangular) analysis regions (tessellations) at each iteration, it cannot use specific traces for correlation through the volume.

A coherence cube from the Boonsville data set was obtained (Figure 20). The delta depositional feature has not been recognized because its variations are subtle; on the other hand, the effects of some deep karstic features are apparent in the coherence volume, even at the Caddo level. As expected, the stratigraphic or structural features stand out if the changes are sharp. Whenever this is the case we can interpret them in a conventional reflection data volume, provided that a coherence cube makes these features more visible for interpretation. Overall, coherence seems to be most useful in configuring depositional systems which involve significant changes in seismic trace pattern, and in interpreting structures because structural deformation often sharply distorts seismic trace patterns.

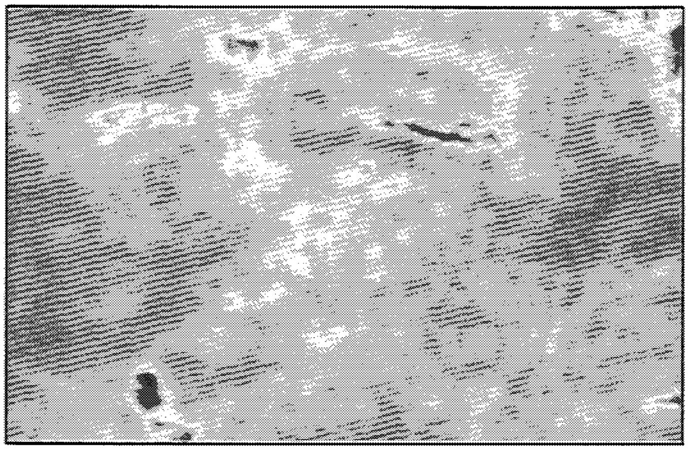

Figure 20: Seismic coherence time slice at 890 ms within the Caddo sequence.

SEISMIC TRACE PATTERN CLASSIFICATION

This approach classifies all seismic traces in a survey to a limited number of classes using mathematical algorithms which vary from conventional cluster analysis to neural network classification. One popular algorithm is based on Kohonen self-organization map (SOM) neural network recognition (Kohonen, 1990; Gurney, 1992). Poupon et al. (1999) demonstrated its usefulness in seismic facies analysis. Basically, in this scheme, each of the model classes corresponds to a discrete class of patterns and the problem then becomes a decision process. All model classes are "self-organized" and updated at each iteration. The final classes are assigned to each trace, each of them is labeled with the corresponding model classes or colors (the lower panel in Figure 21). Notice that changing the time of first sample in the series, due to horizon mistracking, can significantly alter the vector value.

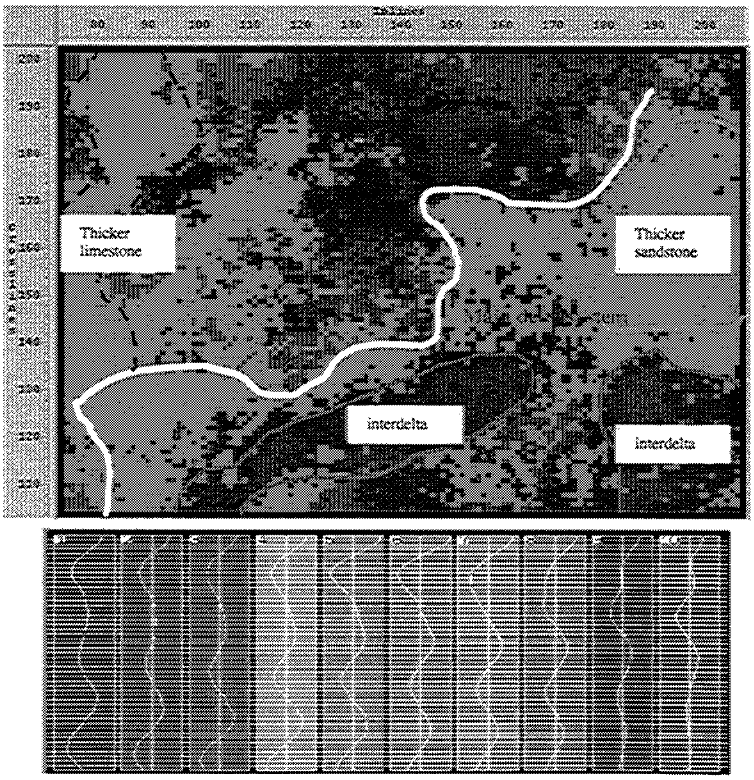

Figure 21: Seismic trace pattern classification and correlated depostional subfacies of the Caddo sequence (upper panel) and ten trace model classes for the seismic trace classification (lower panel, 30 ms window from the top Caddo).

The number of model classes for the neural network needs to be optimized by maximum difference among each model class and maximum correlation factor. Five, ten, fifteen, and twenty classifications were initially chosen with 30 ms tine window, and the ten-classification result provided a map that correlated best as the correlation factor is greater than 70% in most of the study area. The patterns can be correlated to the depositional subfacies (upper panel in Figure 21) if properly calibrated from the well data (Figure 18). Patterns 4-10 were correlated to the delta front and patterns 9-10 were compared to the inter-delta subfacies, patterns 4-8 to the prodelta subfacies. Patterns 5-6 in the west represent thicker limestone zone in the prodelta subfacies. Again, notice that each of the pattern groups is meaningful with depositional subfacies because they were properly correlated to the well-based depositional subfacies.

A NEW AGORITHM FOR SEISMIC FACIES ANALYSIS

We developed a new approach which can: (1) realign a mistracked horizon, (2) discern subtle changes in seismic trace patterns, (3) easily perform pattern recognition for user-specified traces over a survey, (4) provide continuous output values, and (5) combine and visualize the results for multiple trace pattern analysis (posterior-classification).

The algorithm is a modified cross-correlation model, which is a standard method for estimating the degree to which two series are correlated. Consider two series of signals X(i) and Y(i) where i = 1, 2, ... N. The cross-correlation, R, at delay d is defined as

$$R = \frac{\sum_{i}^{N}[(X(i)-X_m)(Y(i-d)-Y_m)]}{\sqrt{\sum_{i}^{N}(X(i)-X_m)^2}\sqrt{\sum_{i}^{N}(Y(i-d)-Y_m)^2}}$$

where X_m and Y_m are the means of the corresponding series and d is the time window for possible horizon mistracking. The denominator in the expressions above serves to normalize the correlation coefficients such that it ranges from –1 to 1. A value of one indicates maximum correlation while zero indicates no correlation. A high negative correlation exhibits a high correlation but of the inverse of one of the series. However, this cross-correlation is focused on the relative similarity of patterns between two time series rather than absolute similarity. Hence, this expression was modified such that it can judge the difference in absolute values within the shape. The modified expression is written below, showing an additional factor that computes for similarity of amplitude on an absolute value:

$$R = \left(\frac{\sum_{i}^{N}[(X(i)-X_m)(Y(i-d)-Y_m)]}{\sqrt{\sum_{i}^{N}(X(i)-X_m)^2}\sqrt{\sum_{i}^{N}(Y(i-d)-Y_m)^2}}\right)\left(\frac{\sum_{i}^{N}|X(i)|-\sum_{i}^{N}|Y(i)|}{\sum_{i}^{N}|X(i)|}\right)$$

This algorithm, as implemented, can also correct for possible horizon mistracking by searching an amount of time (d samples specified by the user) in order to find the highest value for R. The output values for R are continuous from –1 to 1 and provide a value at every trace.

The input of this model consists of seismic data and horizon file as provided by the user. The user needs to define the possible mistracking time window which depends on the confidence of the horizon tracking. The users must then input a trace location of interest, usually a trace at a well with known lithology and/or depositional subfacies. The program will perform pattern processing and output the results, indicating the similarity of all other traces to the one specified trace. Results for one trace at a time are shown in Figure 22.

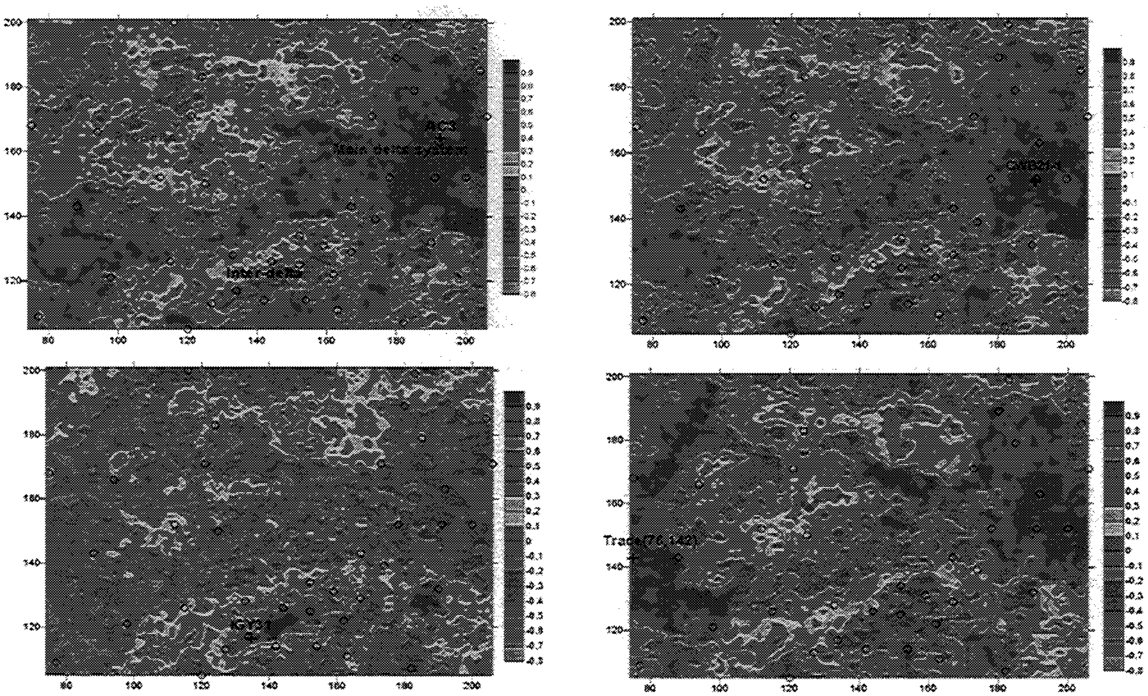

Figure 22: Seismic facies based on new algorithm, using one trace at a time for classification.

Upper left: based on well AC3. *Upper right: based on well CWB21-1.*

Lower left: based on well IGY31 *Lower left: based on trace Inline 76, Crossline 142*

In general, one-trace pattern recognition provides a good seismic facies map as shown in Figure 22 derived from well AC3 only, with R values ranging from –0.8 to 1. Three seismic facies types are readily identified, and by consulting the well-based depositional model (Figure 18), the association with geological facies can be determined with ease. The area of the map with R-value correlation above 0.7 indicates that all the trace patterns are close to the trace pattern at well AC3, which is indicative of the main delta system (notice that the trace patterns were distorted at the northeast corner where karst and faults were developed). Two isolated areas in which the correlation is low or negative indicate the inter-delta subfacies. The coefficient in the north is also low, ranging from –0.3 to 0.7, and is correlated to the prodelta subfacies. Notice that the time window used for the pattern processing is 30 ms starting from the top Caddo sequence, the same size as the previous trace classification window.

Various traces at different well locations were chosen to provide trace pattern processing for different depositional facies. Well CWB21-1, also indicative of the main delta system was used, and the results are almost identical to the facies map derived from well AC3. Well IGY31 recorded the inter-delta subfacies and its corresponding seismic trace pattern correlation results are consistent with the well-based map. Notice that other high coefficient values in the central north area were detected where structural deformation (i.e., karst) was also identified with a strong correlation to this well, a result that is perhaps coincidental.

This algorithm enables us to process any trace specified by the user, whether or not it is at a well location. The trace at inline 76 and cross line 142 is believed to be located within the thicker limestone zone. The high coefficient values indicate the thicker limestone distribution in the west. Notice that the trace patterns in the east where the thicker sandstone reservoirs were developed also correlate with the limestone-based trace. Our algorithm can now be extended to help remove this apparent ambiguity.

Although this new approach is capable of producing reliable seismic facies maps using only one seismic trace for pattern processing, the results from multiple user-specified trace pattern processing can be combined and visualized. The following expression is used to meet this need.

$$R = i * \max(R_1, R_2, \ldots R_i, \ldots, R_n)$$

where i is the order of seismic trace chosen to perform the processing and n is the number of the traces selected. R_i is the correlation coefficient based on the selected trace with the order of i, that is, R_1 may be the correlation coefficient for a trace exemplifying the main delta, whereas R_2 represents the inter-delta, R_3 the limestone, and so no. The resulting R is then chosen as that value, the largest from among the correlations made; it is also assigned a value (*i*) identifying which facies it represents.

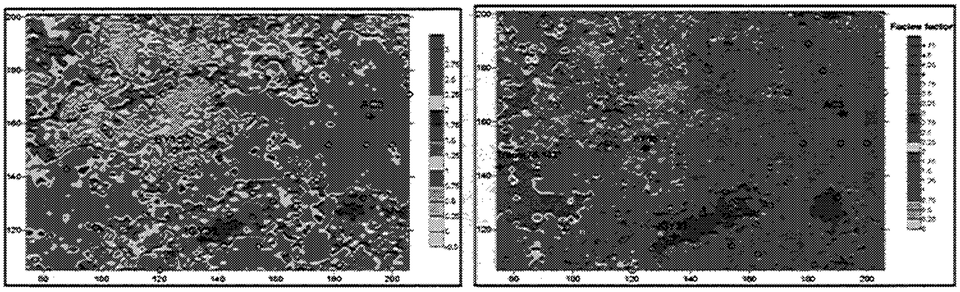

Figure 23: The combined seismic facies using multiple traces.

Left: traces at 3 wells.

Right: limestone and sandstone traces added.

Figure 23 depicts the combined seismic facies obtained from three pattern-processed seismic traces, that is, the traces at well AC3, IGY31 and BY11. These three wells represent the main delta, inter-delta, and prodelta depositional subfacies, respectively. The figure also demonstrates the ability to discriminate the thicker sandstone reservoirs in the east and thicker limestones in the west by adding the additional facies from traces in the known limestone region and thick sandstone region.

CONCLUSIONS

The seismic trace coherence may not able to reveal subtle depositional facies in a thin sequence because of gradual changes of the patterns among the closest neighboring traces. The trace classification approach based on the neural network clustering provided very good results. Our new approach appears to provide some advantages. It provides pattern recognition for multiple user-specified traces (for example, specific "depositional trace" or "oil trace" and "gas trace") over an entire survey. The algorithm has been demonstrated, via the case study, to be robust and promising in defining seismic facies of subtle geological features and predicting thin-bed reservoirs. Notice that, similar to every geophysical output, the geological meaning needs to be defined or verified by geological information. The same correlation values may not represent the same depositional subfacies and the assignment of depositional subfacies depends on our confidence on the geology. More wells, if available, should be selected for the multiple trace pattern processing in those less confident regions.

Boonsville Field 2: Seismic Attributes for Thin-bed Reservoir Prediction

The conventional thin-bed tuning model (i.e., the wedge model) is examined with emphasis on its usefulness or possible pitfalls in thin-bed reservoir prediction of the Caddo sequence, and a new non-linear statistical inversion model built on the generalized regression neural network (GRNN) is applied to the Caddo sequence. Two other seismic inversion models, a non-linear statistical model based on the probabilistic neural network (PNN) and a deterministic model using constrained sparse spike inversion (CSSI) are used to delineate the reservoirs of the Caddo sequence. Our study shows: (1) The conventional thin-bed tuning model is appropriate only if one single thin-bed is developed or multiple widely-spaced thin beds (greater than one quarter of the wavelet length) are present in the sequence of interest. In other words, the model should not be applied for multiple closely-spaced thin beds because of significant destructive interference; (2) All three seismic inversion models were able to identify the thicker reservoir sandstones. However, the resulting details for the thin beds vary. The sparse spike inversion with constraints provided few indications of the thin-bed distribution although it was largely noise-free. The probabilistic neural network (PNN) delineated most of the thin-beds, but produced more noise as well. Our GRNN method predicted the thin beds at 13 out of 20 wells. The GRNN inversion method can be very useful in detecting thin-bed reservoirs in existing fields where a number of wells are available.

INTRODUCTION

Reservoir characterization has historically focused on thick reservoirs (i.e., the thickness greater than seismic resolution). One of the most challenging research problems is to characterize thin-bed reservoirs using 3-D seismic and well data. Based on the quarter wavelength criterion, thin-bed reservoirs range in thickness from a few feet to tens of feet. Tuning effects are observed at this thickness range due to wavelet interference (Widess, 1973; Brown, 1996) and thin-bed reservoirs may not be detected in seismic data or may be difficult to integrate with well data. However, thin-bed reservoir characterization is important as the petroleum industry is devoting greater effort toward tapping more oil from existing fields, many of which are in thin-bed environments.

Progress is being made towards characterization of thin-bed sandstone reservoirs using: (1) instantaneous seismic attributes (Hardage et al. 1994, 1996a; Horkowitz et al., 1996); (2) amplitude (Cooke et al. 1999; Hoover, 1999); (3) frequency decomposition (Partyka et al., 1999); and (4) Bayesian simulation (Gastaldi et al., 1998). To characterize thin-bed reservoirs, however, there are two key factors need to be taken into consideration. One is that a single reservoir layer or multiple widely-spaced reservoir layers are rarely developed in a sequence of interest. Closely spaced thin-bed layers are difficult to predict using the conventional thin-bed tuning model which was generated for a single thin bed between two thick beds. The second one is to remove the tuning effects (detuning). Reflections result from the convolution of a source wavelet with a reflection coefficient, thus representing the boundary between two layers instead of the layer properties. Seismic inversion, which minimizes tuning effects or takes tuning effects into consideration, appears to provide a more robust approach for characterizing thin-bed reservoirs and is the subject of ongoing research (Salleh et al., 1999; Torres-Verdin et al., 1999; Riel, 2000; Pennington, 2001).

Two approaches can be used to recover acoustic impedance from seismic data. One technique is to remove or minimize the tuning effects by applying a deconvolution model. This is the conventional deterministic seismic inversion. A few theoretical methods have emerged since

1980s, such as linear programming (Taylor et al., 1979; Cooke, et al., 1983; Oldenburg et al., 1983), maximum-likelihood or sparse spike inversion (Chi, et al., 1984), and more recently, constrained sparse spike inversion (Debeye et al., 1990). All these methods resolve the components of the convolutional model in each seismic trace.

The other alternative is to not remove the tuning effects from a seismic data set, but to establish a statistical relationship between seismic attributes and impedance (multi-attributes analysis, Hampson et al., 2001). Non-linear statistics are used to describe the relationship between attributes and acoustic impedance as the relation between them is complicated. Neural networks are most often used to construct this non-linear relation. A couple of neural networks that have been in use for seismic inversion are the multi-layer feed-forward neural network (MLFN) (Liu, et al., 1998) and probabilistic neural network (PNN) (Hampson, et al., 2001). Non-linear relationships imply that more than one step or expression is required to simulate the observations from the known inputs, in contrast to one step in linear relationship. Each layer consists of nodes and weights. The nodes are connected with weights and the neural network process finds the optimal weights between the nodes by training a data set. Then, the statistical model is applied to simulate an entire data set.

Our study area is again the Boonsville Field, Fort Worth Basin of the north central Texas. In this study, we examine the conventional thin-bed tuning model, apply a new generalized regression neural network model, and perform a comparison study with two other inversion models with a focus on the prediction the thin-bed reservoirs.

EVALUATION OF THE CONVENTIONAL THIN-BED TUNING MODEL

The conventional thin-bed tuning model was derived from a wedge model. Widess (1973) demonstrated the interaction of the top and base reflectors of a thin bed wedge, illustrating that amplitude increases as thin-bed thickness increases until the amplitude of the composite wavelet reaches a maximum for a bed thickness of one-quarter wavelength. Clearly, the bed thickness at which these phenomena occur depends on the shape of the wavelet or its frequency band and the velocity of the reservoir of interest. For instance, one-quarter of the wavelength is approximately 50 feet for the Boonsville Field data set, given 12000 ft/s as the average velocity of the Caddo sequence and 57 Hz as the dominant frequency of the seismic data (Figure 24). It is assumed that the post-stacked (summed) amplitude represents the zero-offset amplitude; that is, AVO effects were ignored.

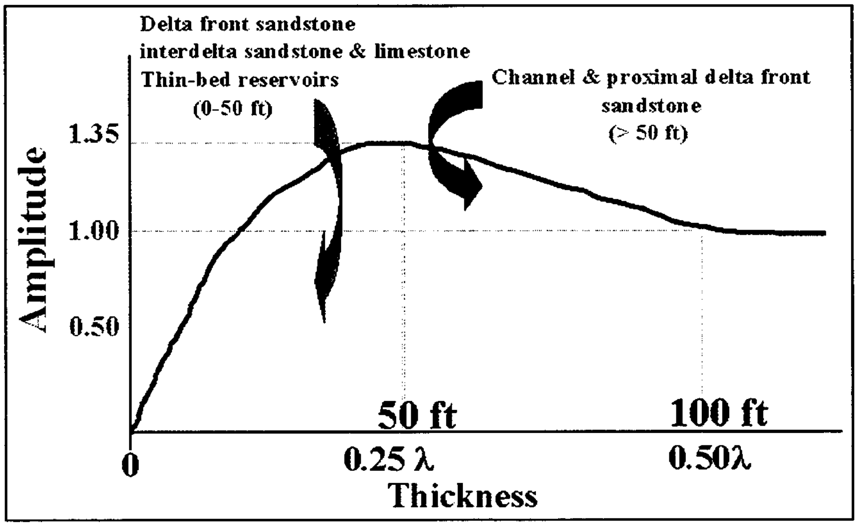

Figure 4: Conventional thin-bed tuning model with notations for our data set.

The thin-bed tuning model has been widely employed to predict thin-bed reservoirs. A number of case studies have been published during the last decade (Brown, 1996; Hoover et al., 1999; Cooke et al., 1999). In reality, however, a sequence of interest is rarely developed by a single reservoir layer or by multiple widely-spaced reservoir layers. Closely spaced thin-beds will present a challenge in predicting reservoir distribution using the model derived from a single wedge model. Notice that multiple thin beds are closely spaced if the vertical distance between two thin beds is less than one-quarter of a wavelength. Therefore, two or more closely-spaced thin beds will destructively interfere, and thus will not obey the simple relationship between amplitude attribute and reservoir thickness developed for a single thin bed.

Two-dimensional (more precisely 1.5-D) seismic forward modeling was implemented to better illustrate the multiple closely spaced model. The wavelet applied in the modeling is a zero-phase Richer wavelet with the same dominant frequency of 57 Hz as that from the seismic data. The velocities of the sandstone, limestone and shale, based on the statistical results from the acoustic well logs, are 14200, 15200, and 11800 ft/s, respectively. Amplitude attenuation demonstrates the destructive interference between the two closely spaced thin sandstones in a shale-rich sequence (Figure 25).

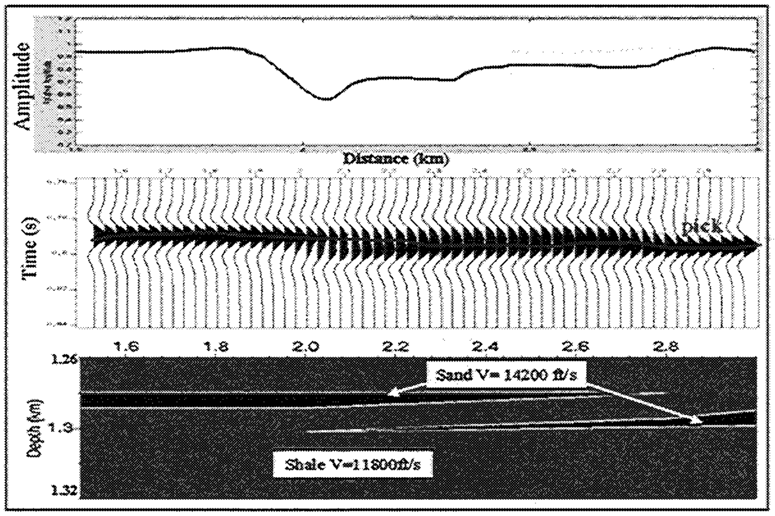

Figure 25: Modeled seismic response showing amplitude attenuation where two closely-spaced thin sandstone layers are developed.

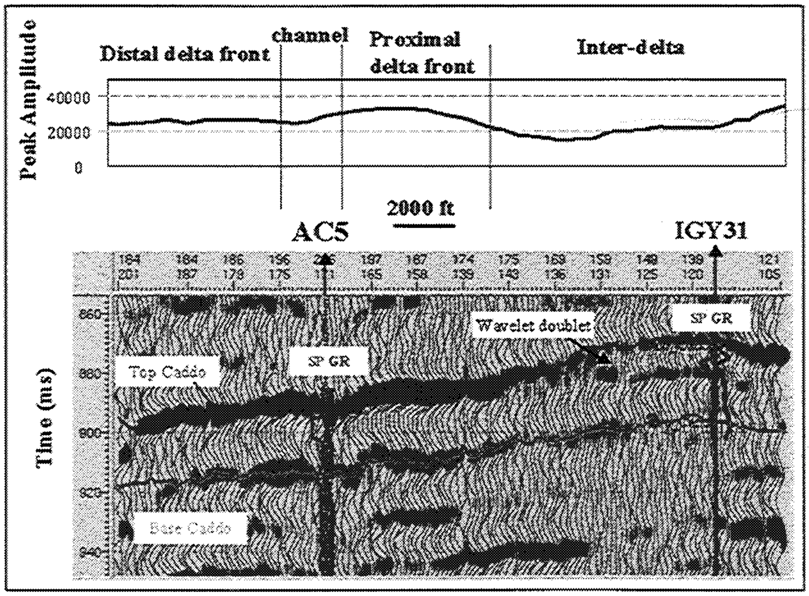

Figure 26: Seismic features through the main delta system showing amplitude decrease and wavelet doublet in interdelta subfacies.

A seismic traverse line through the main delta system of this study area (oil producing area) is shown in Figure 26. The amplitude attenuates in the inter-delta subfacies where the thin limestone and sandstone are closely spaced. To avoid using biased amplitudes due to a possible peak mistracking, the RMS amplitude computed over 20 ms time window below the top Caddo horizon was used instead of single point amplitude. The relationship between RMS amplitude and the summed thickness of the sandstone and limestone at 37 wells is shown in Figure 27a. The summed thickness of two types of rock was used because the sandstones cannot be separated from the limestones utilizing the amplitude and/or acoustic impedance alone. It clearly does not agree with the conventional thin-bed tuning model and should not be used for approximating the thickness of sandstone and limestone.

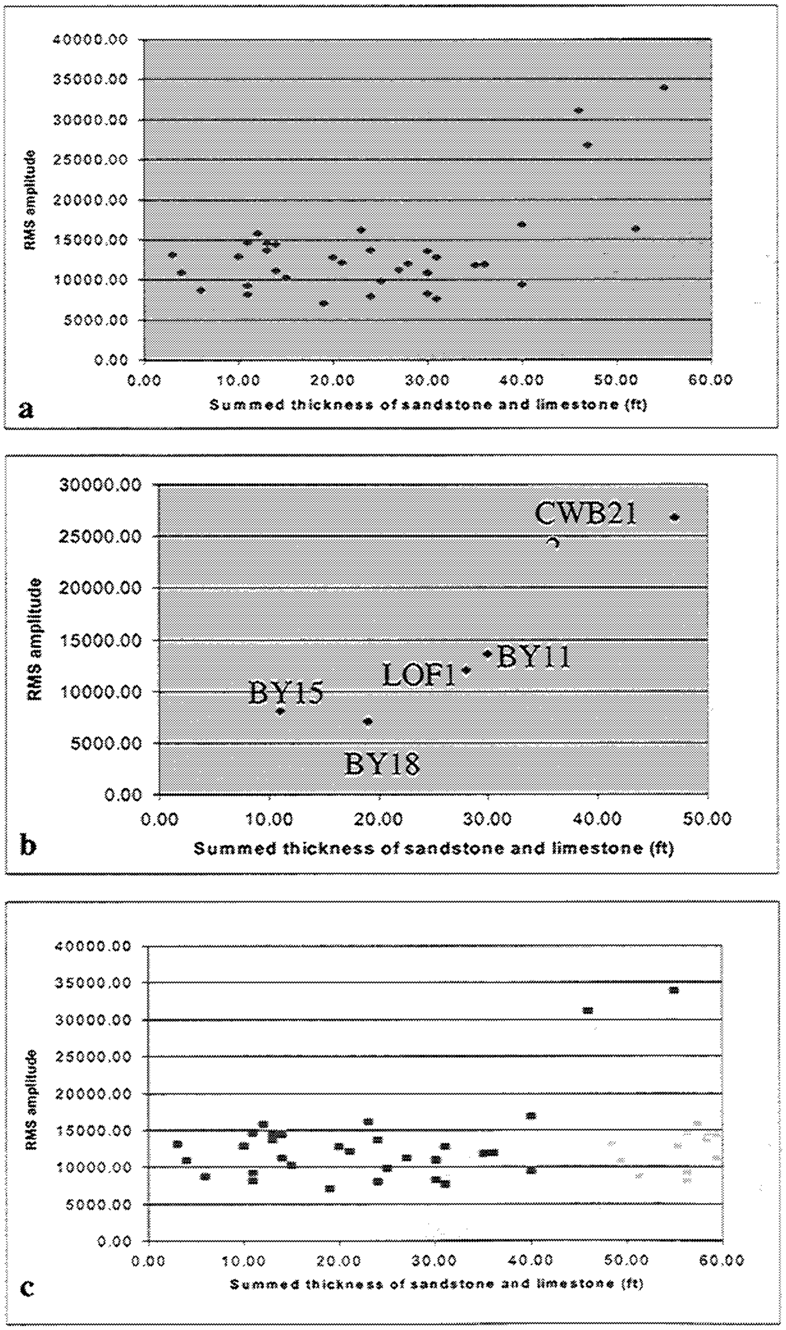

Figure 27: RMS Amplitude plotted against summed thickness of sandstone and limestone.

(a) for 37 wells

(b) for a single thin bed or multiple widely-spaced thin beds

(c) for multiple closely-spaced thin beds.

By interpreting the sandstone and limestone layers and the shale thickness between them, two groups were categorized for this data set: multiple closely-spaced layers and single layer or widely spaced layers. The single layer and widely spaced layers are consistent with the thin-bed tuning model because there is no significant destructive interference between multiple thin beds. The correlation of the amplitude of the second group against the summed thickness of layers is shown in Figure 27b. This suggests that the amplitude increases with increasing thickness at least up to one-quarter wavelet length (50 feet). Therefore, the thin-bed tuning model works for single layer or widely spaced layers (Figure 27b), but fails for the closely spaced thin beds (Figure 27c).

In general, the conventional thin-bed tuning model does not often apply because a single reservoir and/or multiple widely spaced reservoirs are rarely developed in a sequence. As a consequence, seismic inversion, which shows more promise in predicting reservoirs, will be investigated in this chapter.

GENERALIZED REGRESSION NEURAL NETWORK INVERSION

The prior study showed that the conventional thin-bed tuning model is not applicable due to destructive interference among multiple closely-spaced layers. Here seismic inversion models are employed to derive layer properties (acoustic impedance in this paper). One of our research goals is to use a novel non-linear generalized regression neural network (GRNN) inversion model to predict the thin-bed reservoirs. The results will be compared with two existing inversion software models, that is, the probabilistic neural network (PNN) and constrained sparse spike model (CSSI).

GRNN inversion model

In this study, a GRNN inversion algorithm was developed and tested on the Boonsville data set. Chen (1996) described the relevant mathematical model in detail. The GRNN algorithm provides estimates of continuous variables and converges smoothly to the underlying regression curve (in case of 1-D). It features instant learning and always gives a smooth transition from one observed value to another. The GRNN model is primarily derived from the radial basis function (RBF) which is a neural network concentrated on localized basis or potential functions and iterative function approximation. This function requires more neurons than standard feed-forward back-propagation networks, but it can be designed in a fraction of the time it takes to train standard feed-forward network such as MLFN. Our GRNN model consists of two layers; the first layer is the hidden RBF and the second layer is a linear regression function.

High-cut or low pass filtering should be applied to cut off the very high frequency component of the impedance from wells in order to "upscale" to the seismic frequency from full band frequency of well data. The neural network technique tries to build a non-linear relationship between seismic attributes and impedance by "forcing" processing to incorporate all the information as possible even if some of the "information" is noise. High-cut filtering smoothes impedance curves and ensures that the relationship is not far beyond the seismic resolution. It also reduces some noise. We applied a 120 Hz high-cut filter (the maximum frequency component) to the impedance logs. Four basic attributes (amplitude, envelope, instantaneous phase, and instantaneous frequency) were used as an input set to the GRNN neural network. A convolution model was applied to better link these attributes to the acoustic impedance. This convolutional operator is consistent with the geophysical model and adds more variables to the input vector, thus improving the accuracy of the neural network (Hampson et al., 2001).

Application of the GRNN model to the Boonsville Field data set

This GRNN inversion approach was applied to the Boonsville Field data set and six wells (AC5, BY11, BY13, BY18D, CY9, and IGY31) were used for the training data set because their synthetic curves can be tied to the seismic traces without "squeezing and stretching". The correlation coefficient between inverted and actual impedance at the wells in the training set is 0.84. A blind test was conducted in which one well at a time was removed from the training set; the inversion result at the associated seismic trace was compared with the impedance from that well, which obtains coefficient of 0.52. The inverted impedance can be used to predict the presence of the sandstone reservoirs by interpreting high impedances of 32000 ft/s*g/cc as a base value (Figure 28). The impedances of the sandstone reservoirs and limestones are greater than the base value whereas the impedance of the embedding shale is less than the base value.

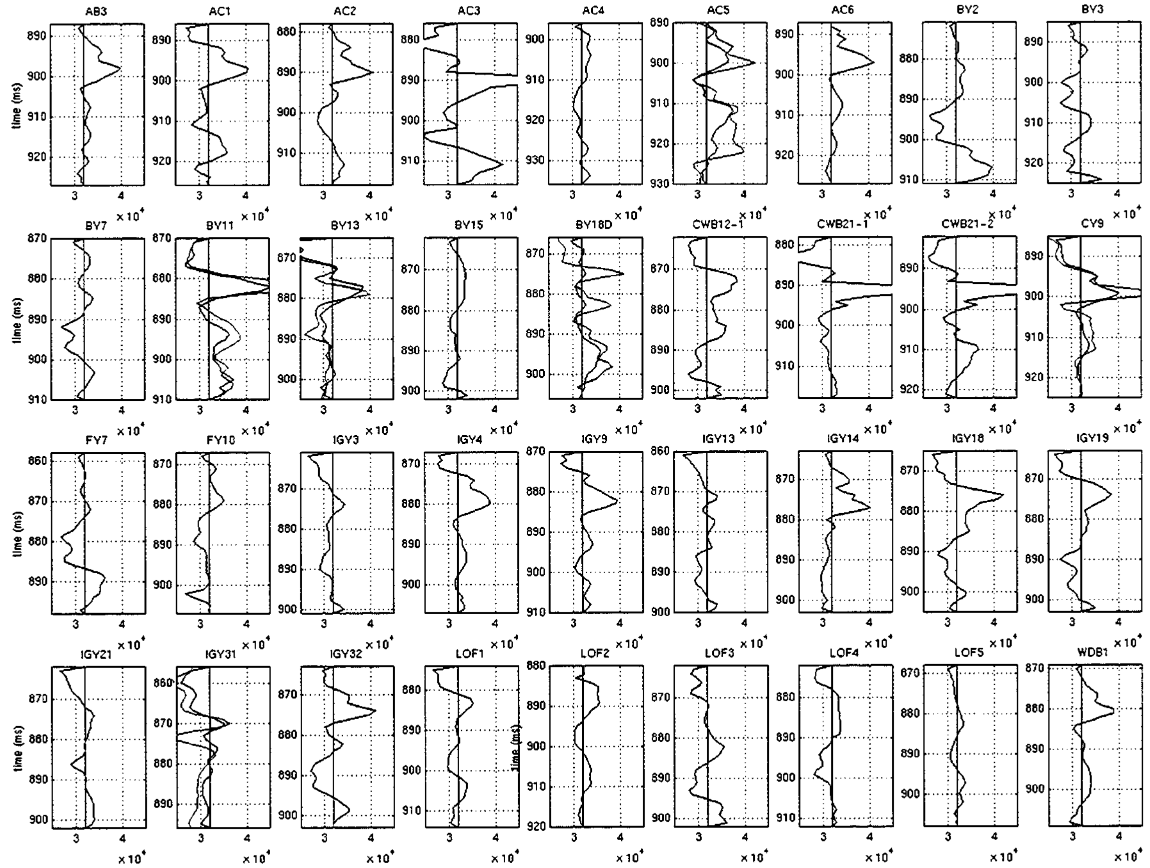

Figure 28: Inverted impedance curves using the GRNN model at 36 wells

*(the base line represents 32000 ft/s*g/cc, and the original acoustic impedance curves are shown at the six wells for which they could be computed, in red.*

Our GRNN inversion made correct predictions at all well locations in the proximal delta front and distal channel (wells AC3, CWB21-1, CWB21-2, and AC5) where thicker sandstones were developed and inverted impedance is more than 39000 ft/s*g/cc. The inverted impedance at well AC4 is around 32000 ft/s*g/cc and consistent with the fact that no reservoir and only thin shaly limestones were deposited. At well BY2 and BY3 where only sandy shales or shaly sandstones are present, the inverted impedance is lower than or near to 33000 ft/s*g/cc. The inverted impedance at the well FY10 ranges from 33000 to 34000 ft/s*g/cc and agrees with the presence of the shaly sandstones at that transition interval from the delta front to prodelta subfacies. At well FY7, sandy shale was found and its inverted impedance is lower than the base value. All of these show that the inverted impedance was able to identify the presence of the thicker sandstones and limestones.

Twenty wells out of the 30 blindly tested wells are located in the distal delta front and interdelta subfacies (AB3, AC1 AC2, AC6, WDB1, LOF1, LOF2, LOF3, LOF4, LOF5, CWB12-1, IGY3, IGY4, IGY9, IGY13, IGY14, IGY18, IGY19, IGY21, and IGY32, see Figure 28). The GRNN approach was able to detect the thin-bed sandstone and/or limestone at 13 out of 20 wells. The model was not able to identify the thin-bed sandstones and limestones at 7 wells in the distal delta front (LOF1, LOF3, LOF4, LOF5, IGY3, IGY13, and IGY21). The high impedance layers (limestones) in the prodelta subfacies were correctly predicted at wells BY11 and BY13, but not at wells BY18D and BY15.

Two inverted impedance cross sections (crossline 125 and 171) are depicted in Figure 29. The high impedance is highlighted in the east, center and west, indicating the main delta sandstone reservoirs, minor distributary channel sandstone, and limestone, accordingly. Notice that the inverted impedance is relatively low at some traces in the center of the crossline 171 (the "doublet wavelet" region). The impedance cube with different opacity cutoffs is shown in Figure 30 which highlights the thicker sandstone in the east (proximal delta front) and the thicker limestone in the west (prodelta subfacies), minor distributary channel sandstone in the center, thin beds in the east and south, and distal delta front sandstones and/or limestones in the east. The inversion technique also easily reveals the lateral discontinuity of the sandstone reservoirs and limestones in the Caddo sequence.

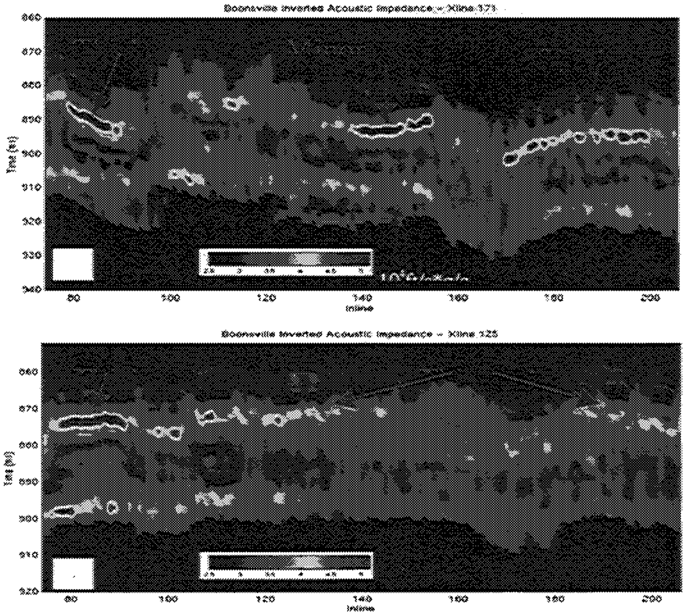

Figure 29: Crosslines 171 (a) and 125 (b) of the inverted impedance data using the GRNN model indicating sandstone and limestone as higher impedances.

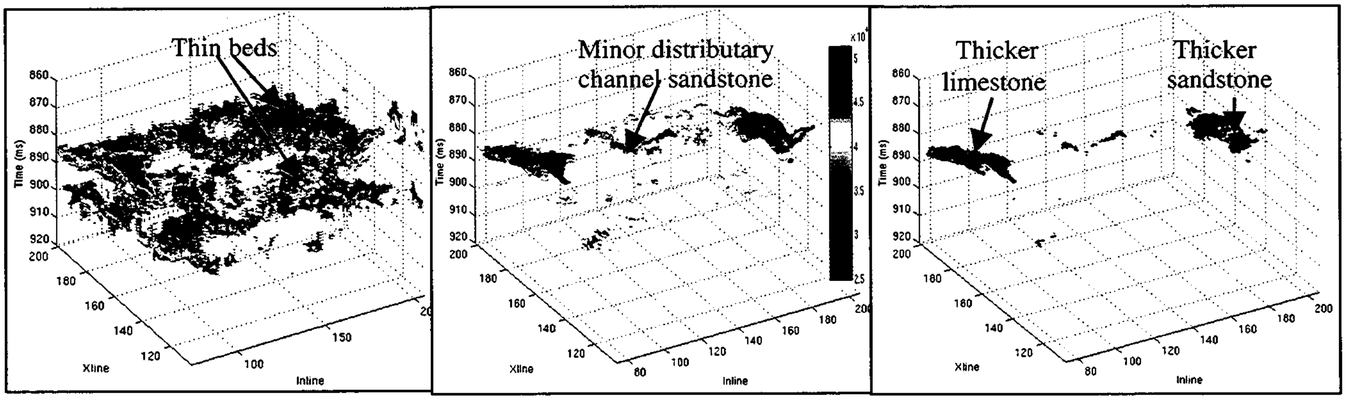

Figure 30: Inverted impedance volume (GRNN model) with different opacity cut-offs.

*Left: 32000 ft/s*g/cc* *Center: 36000 ft/s*g/cc* *Right: 39000 ft/s*g/cc*

OTHER INVERSION MODELS

Probabilistic neural network inversion (PNN)

The PNN inversion is a two-layer neural network with the hidden layer as its first layer. According to Hampson et al. (2001), this hidden layer might be similar to the RBF in the previous GRNN model because the Gaussian basis function is used in this layer to compute the distances from the input vector to the training vector (Hampson et al., 2001). However, the second layer is different in that it utilizes a compete transfer function based on the probabilities, instead of a regression function in the second layer of the GRNN model.

The PNN inversion proceeded in the following steps: (1) wells were tied to seismic traces, (2) training and validating were preformed on the nine pre-selected wells (AC5, AC6, BY11, BY13, BY18D, CY9, IGY14, IGY19, and IGY31) in an effort to establish a neural network relationship between the seismic attributes and actual acoustic impedance, and (3) the inverted impedance data was analyzed. The training results with correlation coefficient of the inverted and actual impedance is 0.86, with a validation coefficient of 0.56, implying the prediction accuracy is about 0.56. This prediction accuracy is close to our GRNN model of 0.52.

Figure 31 shows the impedance slice 6 ms below the top Caddo horizon and demonstrates the main geological features of the Caddo sequence. The highest impedance areas (in red) in the east and west represent the thicker sandstone reservoirs and limestones, respectively. A northwest-oriented zone with the inverted impedance of 33000-35000 indicates the minor distributary channel (no well was drilled yet). In the east and south, the intermediate impedance, ranging from 32000 to 37000 ft/s*g/cc, indicates the presence of the thin-bed sandstone and/or thin-bed limestone, corresponding to the distal delta front and interdelta subfacies. The inverted impedance is slightly lower than the actual impedance in those regions because of the truncation related to the scale problem; however, it is still higher than the inverted impedance in the north-central parts where no clean sandstone and pure limestone were deposited. Notice that some isolated thin-bed limestones in the prodelta were not predicted, for instance, at well BY15.

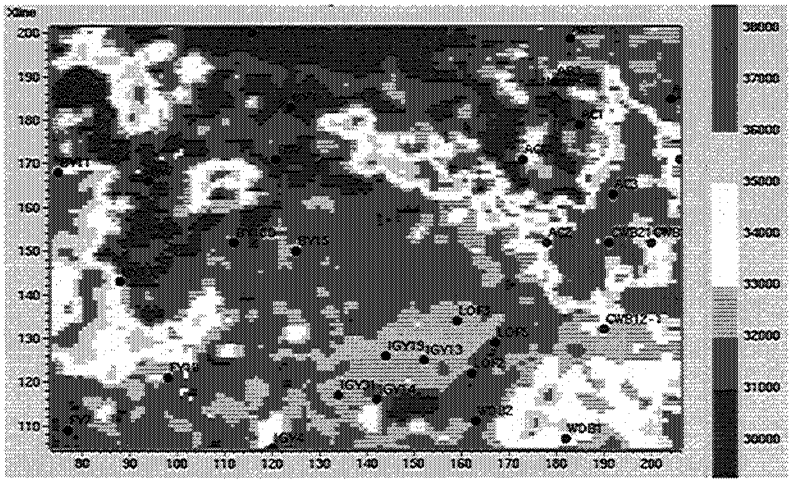

Figure 31: Inverted impedance data using the PNN model.

Time slice 6 ms below the top Caddo horizon, showing the distribution of high impedances.

One representative crossline (117) is shown in Figure 32. Notice that high impedance, ranging from 37000 to 45000 ft/s*g/cc, indicates the thicker sandstone reservoirs and/or limestone non-reservoirs and the intermediate impedance from 33000 to 37000 ft/s*g/cc represents the thin-bed sandstone reservoirs and/or thin-bed limestone non-reservoirs because of the truncation. Crossline 117 illustrates the high impedance layers in the east and center. They represent the thin-bed sandstone reservoirs and the closely spaced thin-bed sandstone reservoirs, respectively (compare with the well-based depositional model, Figure 18). The thicker limestones in the west were not revealed in crossline 117 while the GRNN did recognize them (Figure 30). This also demonstrates that the sandstones and limestones are heterogeneous.

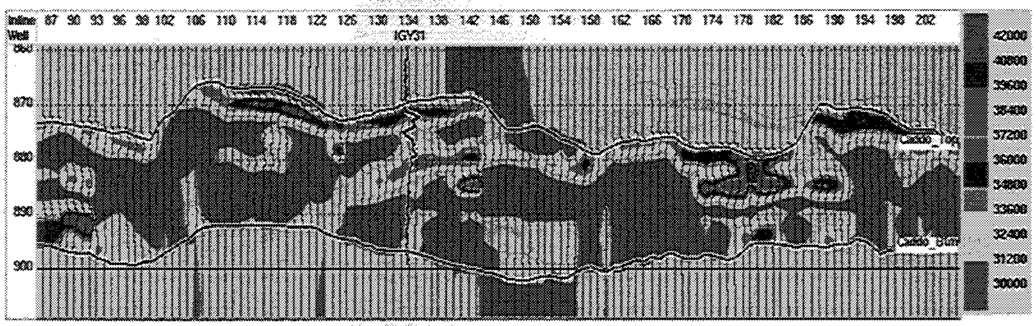

Figure 32: Crossline 117 of the invertedimpedance volume using the PNN model.

It is difficult to discriminate the sandstone from the limestone using the inverted impedance alone. However, they can be separated by knowing the depositional model already constructed using well and seismic data (see our separate paper). In order to interpret the limestone and sandstone from the impedance cube, the cutoff of 32000 ft/s*g/cc was obtained on the basis of well data. The thicknesses from 37 wells are shown in Figure 33, against the thickness estimated from the inversion results. This relationship demonstrates the advantage of using impedance or layer properties over using the amplitude attribute for thin bed estimates (see Figure 27a). The estimated sandstone reservoir distribution is illustrated in Figure 34. Note that the limestones in the west were manually removed, but we was not able to separate them from the sandstones in the interdelta (i.e. in the south) and western margin of the main delta system. This figure shows that no reservoir sandstone was developed in some parts of the main delta system, supporting the lateral heterogeneity of the thin-bed reservoirs in the shale-rich Caddo sequence.

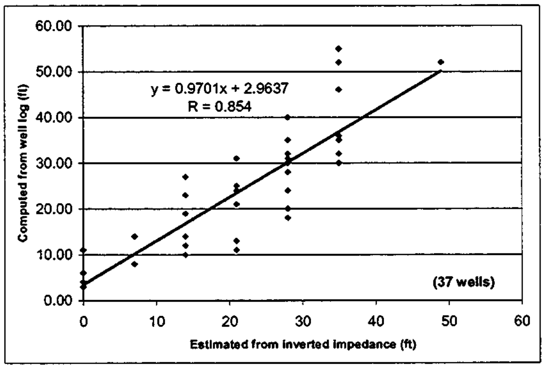

Figure 33: Actual sandstone and limestone thickness plotted against predicted thickness from seismic inversion (PNN model)

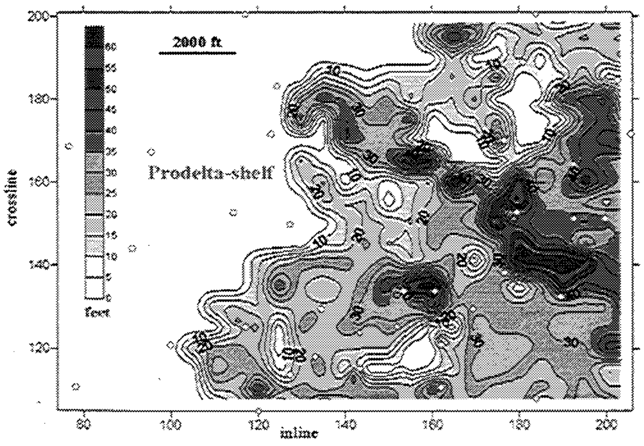

Figure 34: Estimated sandstone thickness of Caddo main delta system (PNN model)

Note: the limestones in the west were removed manually in this example)

CONSTRAINED SPARSE SPIKE INVERSION (CSSI)

The CSSI inversion model is based on the convolution and deconvolution model. It involves two fundamental techniques: wavelet estimation and balanced spike and wavelet deconvolution (Chi, et al., 1984; Yilmaz, 1987; Russell, 1988; Debeye et al., 1990). The CSSI inversion was applied to the Boonsville data set. Six main procedures were followed in performing the CSSI inversion, with a focus on the quality control: (1) building earth model, (2) estimating wavelets based on 5 wells (BY11, BY18D, CY9, AC5, and IGY31), (3) conducting constraints, (4) inverting trace by trace, (5) merging traces, and (6) interpreting inverted impedance data. The inverted impedance agrees with the actual impedance with the correlation coefficient of 0.72 for the Caddo sequence (Figure 35).

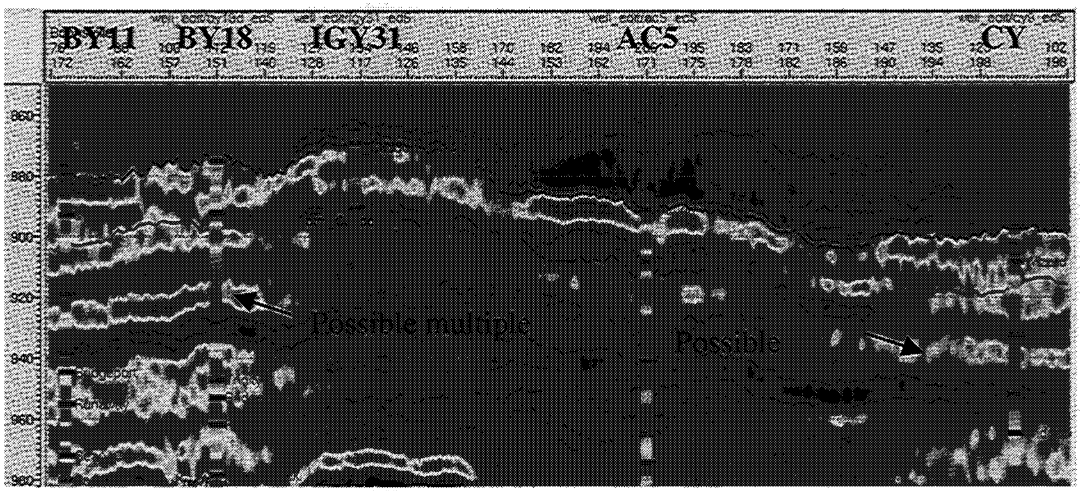

Figure 35: Traverse line showing the inverted impedance using CSSI model and agreement with well data (the five wells indicated were used to estimate the wavelet and provide constraints).

A high quality match between inverted and actual impedance layers would allow us to estimate the sandstone and limestone by tracking the high impedance layers. However, the layers with the impedance higher than 33000 ft/s*g/cc in the Caddo sequence were found in the entire survey including the prodelta subfacies (Figure 36, top). Furthermore, the inverted impedance in most of the distal delta front and inter-delta subfacies is the lowest, which prevents us from identifying the thin-bed sandstones and limestones. For instance, the inverted impedance at well BY3 and BY3, where no sandstone and limestone were interpreted, is not lower than the impedance in the delta front area. A variety of opacity cut-offs was explored as shown in Figure 36, which reveals that thicker sandstone and/or limestone were able to be delineated (Figure 36, bottom). The CSSI inversion provided few indications of the thin-bed reservoir distribution. The parameter λ may be varied in order to obtain more thin-bed results, but at the risk of inducing additional noise.

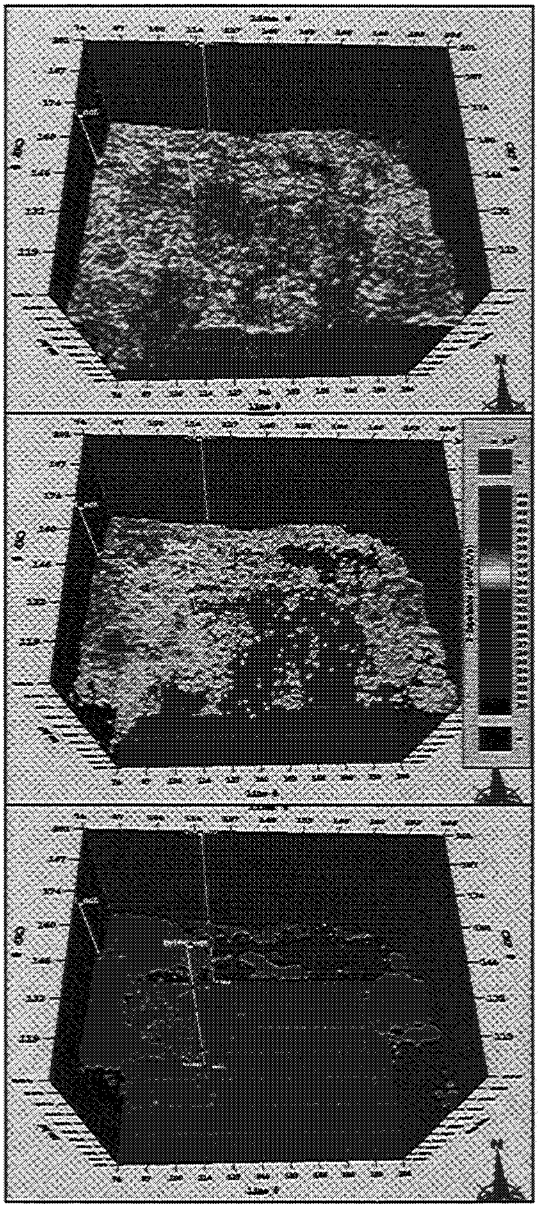

Figure 36: Inverted impedance volume using the CSSI with different opacity cut-offs.

*Top: 33000 ft/s*g/cc*

*Center: 36000 ft/s*g/cc*

*Bottom: 39000 ft/s*g/cc*

CONCLUSIONS

Evaluation of the conventional thin-bed tuning model (wedge model) shows that it is appropriate only if one single thin-bed is developed or multiple widely spaced thin beds (greater than one quarter of the wavelet length) are present in the sequence of interest. In other words, the model should not be applied for multiple closely spaced thin-beds because of significant destructive interference.

All three inversion models were able to identify the thicker reservoir sandstones and non-reservoir limestones. However, the resulting details for the thin-beds vary. The Boonsville case study shows that our GRNN inversion detected the thin-bed sandstone and limestone at the rate of 13 out of 20 wells. The PNN inversion was also able to predict most of the thin-beds and enhanced the thickness estimates of the thin-bed sandstone and limestone, but the inverted impedance is nosier than that using the GRNN model. The deterministic approach with constraints (CSSI) shows a good agreement of the inverted impedance with the actual impedance logs as a whole, but provided few indications of the thin-beds, perhaps due to our avoidance of noise. For this post-stack data set, it is implicitly assumed that the stack volume represents zero-offset reflections, an assumption that may cause some systematic errors in the deterministic inversion.

Non-linear statistical inversion focuses on both amplitude and trace shape in the convolution window. This method always forces the system to construct a relationship between multiple seismic attributes and acoustic impedance. As a result, AVO effects have less influence on it. It is more robust in delineating thin-bed reservoirs where multiple wells are available. However, the statistic inversion methods require a number of wells. The GRNN inversion should be very useful in detecting thin-bed reservoirs in existing fields where a number of wells are available.

Teal South, Offshore Louisiana, Gulf of Mexico

The Teal South field lies offshore of Louisiana about 70 miles south of Morgan City. It is a fairly small field, until recently operated by Texaco, that produces from more than one horizon. Texaco chose that field for a time-lapse study because it was expected to deplete quickly and could provide useful information for evaluating time-lapse techniques within a few years. After their initial time-lapse study, Texaco offered the opportunity to study ocean-bottom multi-component seismic time-lapse techniques to the industry in general, through a consortium organized by the ERCH. That consortium has grown to include a number of producing companies and service companies, as well as a few universities (additional information can be found on the ERCH web site: http://www.erch.org). Our involvement in the project, supported through this contract with the DOE, has been to analyze the 'legacy' seismic-streamer data for the physical basis of the seismic attributes (this is a conventional 'bright-spot' play), and to predict the observations expected from the time-lapse studies. If we have calibrated the attributes properly, our predictions should be viable; if the predictions are incorrect, then we must not have calibrated the attributes appropriately.

We have accomplished this objective, and much more, as demonstrated in the following part of this report.

INTRODUCTION AND FIELD CHARACTERISTICS

Geophysicists conduct time-lapse seismic surveys in order to find out what is incorrect in the reservoir model, in a way similar to the production history matching familiar to reservoir engineers as they look for improvements to the model. This being the case, it is difficult to determine in advance of monitoring just what it is we should be monitoring, and survey that are designed specifically to test one feature of a reservoir model may be missing other important features. In this part of the report, we present a set of very surprising results from the Teal South Time-Lapse Multi-Component (4D-4C) study, in Eugene Island Block 354 in the Gulf of Mexico. We will show that time-lapse seismic observations have revealed that an undrilled reservoir near a producing reservoir is exhibiting time-lapse changes consistent with expansion of a free gas phase, and that this implies that oil is being lost through the spill point, never to be recovered, even if that reservoir is eventually drilled for production.

The Teal South 4D-4C study has provided seismic data sets covering three different times: one time prior to production ("legacy" streamer data), and at two times after production (Phase I and Phase II, each using 4-component ocean-bottom cables). The project, initiated by Texaco, has been continued through a consortium organized by the Energy Research Clearing House, and some of the results of this project have been described in previous articles in TLE (Ebrom and others, TLE, March 2000; Entralgo and Spitz, TLE, June 2001). Although this project was originally designed specifically as a test of seismic technologies, it has evolved into a test of petrophysics and reservoir models as well.

The field of most interest to the study is the so-called "4500-ft" reservoir (labeled "A" on Figure 37); it quickly generated free gas under production, having been near bubble point at discovery, and appears to have developed a zone of encroached water as well as a gas cap. Reservoirs with an initial liquid expansion drive mechanism undergo an initial very rapid decrease in pore pressure, followed by a less rapid, but nonetheless steady, continued decline in pressure during the solution-gas-drive phase of production (with moderate water drive in this case). The production history of the 4500-ft reservoir is summarized in Figure 38. Conventional wisdom had predicted that the seismic response of the 4500-ft reservoir would consist of continued 'brightening' of this Class III AVO reservoir with production as the gas saturation continuously increased. A prediction was made (Pennington, paper RC 3.5, 2000 SEG meeting extended abstracts) that the situation would actually be quite a bit more complicated: due to the fluid-substitution effects alone, there should be continued brightening at all offsets; but, because there is also an increase in effective confining pressure as a result of pore-pressure decline during production, this bright spot should dim at near offsets after the initial brightening from the exsolution of free gas. This type of petrophysical behavior has also been proposed by Landro (GEOPHYSICS, May-June 2001) and Bentley et al (paper 7.3, 2000 SEG meeting extended abstracts).

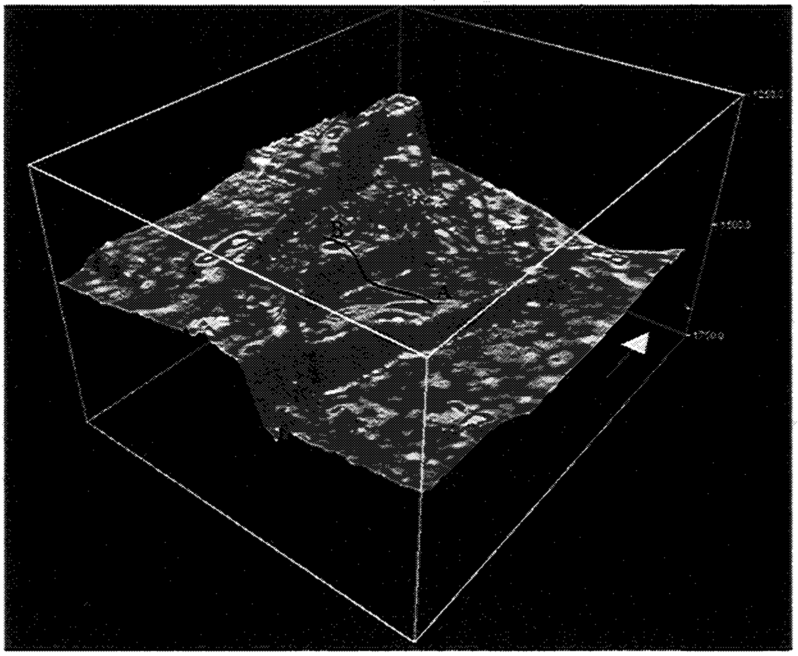

Figure 37: 3D perspective view of the sand structure containing the currently producing '4500-ft' reservoir, labeled A, as well as nearby undrilled potential reservoirs, including the "Little Neighbor" labeled B. The arrow points North; the box outlining the volume extends from 1250 ms to 1750 ms in two-way travel time, and is roughly 8000 ft (2500 m) on each side. Hotter colors indicate larger negative amplitudes on the migrated legacy (pre-production) seismic data.

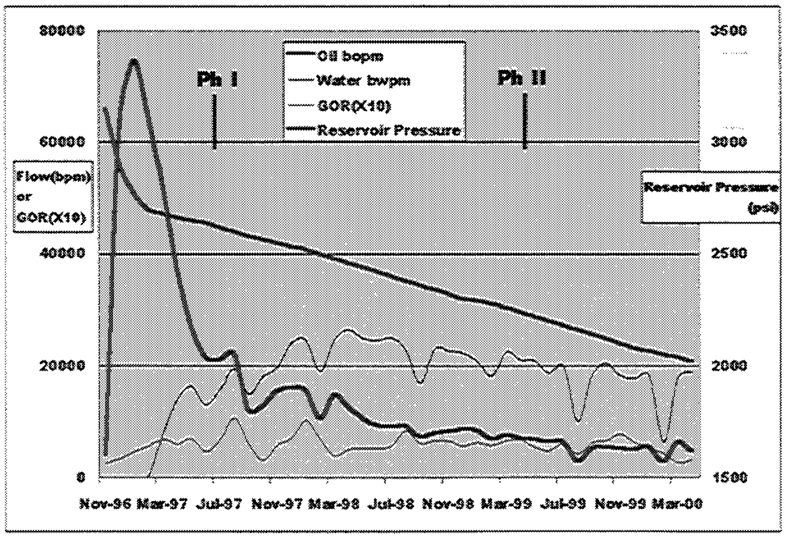

Figure 38: Smoothed production history of the 4500-ft reservoir; the Oil flow rates (in bbls of oil per month), water flow rates (bbls of water per month), and Gas-Oil-Ratio (GOR multiplied by 10) are all read from the left axis, and the reservoir pressure (in psi) is read from the right axis. The reservoir pressure is simplified from the results of a reservoir simulation conducted by personnel at Heriot-Watt University. Times of the ocean-bottom time-lapse surveys Phase I and Phase II are indicated.

ROCK PROPERTIES DETERMINATION

In order to test and calibrate the model used in time-lapse seismic petrophysical predictions, we first needed to know the properties of the rocks in situ. The log data were inconclusive, and it was necessary to establish confidence in our petrophysical model through inversion of the legacy seismic data for acoustic impedance (see Figure 39). The final result was a model in which fluid-substitution, using Gassmann theory, was consistent between the oil and water legs of the 4500-ft sand – that is, when we used the values obtained for acoustic impedance in the water sand, and made some simple assumptions for dry-frame Poisson's ratio (which, in this case, were not critical), we were able to predict the values for acoustic impedance observed in the oil sands. Thus, we had a set of rock properties on which to base our predictions for seismic response during production, at least to the degree of accuracy required here.

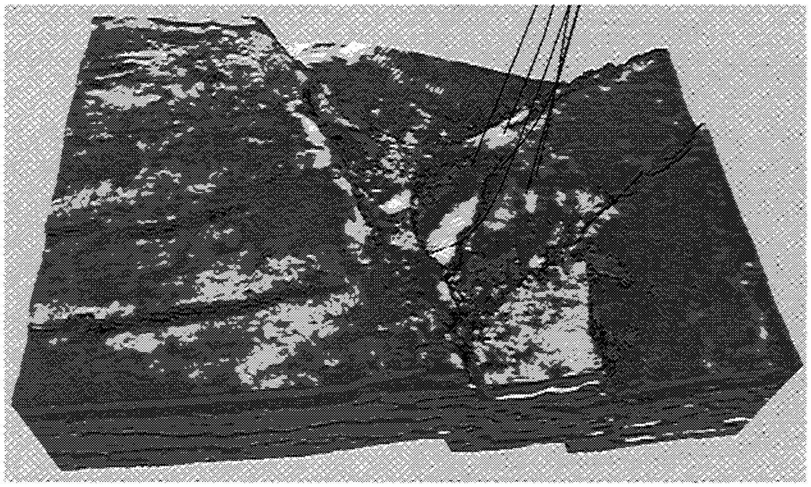

Figure 39: Inverted (legacy data) volume showing acoustic impedance 12 ms below the top of the tracked 4500-ft horizon, inside the reservoir intervals. The green color indicates high impedances (shales), red colors indicate intermediate impedances (water sands), and the yellow colors indicate low impedances (oil sands).

At the same time, additional nearby reservoirs were identified (such as the "Little Neighbor" labeled "B" in Figure 37), and were occasionally of interest to the investigators in the Teal South consortium. The production history from the producing fields was known, yet some effects were consistently showing up in the undrilled reservoirs. For example, Figure 40 shows a difference image obtained by subtracting the amplitudes on the 4500-ft horizon between Phases I and II.

Figure 40: Time-lapse difference mapped on the 4500-ft horizon, showing the change in amplitudes of the stacked seismic data between Phase I and Phase II, the two OBC time-lapse surveys. The 4500-ft reservoir and the Little Neighbor reservoir both show significant changes indicated by the blue and green colors, although only the larger 4500-ft reservoir is under production. (Image provided by W. Haggard, C. Vuillermoz, S. Spitz, and P. Granger of CGG, presented to the ERCH consortium in August, 2000.)

The model for fluid substitutions due to changing gas saturation and for frame stiffening due to increased confining pressure indicated (Figure 41) that the P-wave velocity should initially decrease and then increase significantly during production, while Poisson's ratio should continually decrease. This scenario results in an amplitude-versus-offset effect (Figure 42) that includes an initial brightening at all offsets, followed by a dimming at near offsets and a continued brightening at far offsets. [The model used in calculating the frame stiffening is an extension of one presented by Pennington, Green, and Haataja at the AAPG Annual Meeting, 2001, and was developed by Aaron Green (M.S. Thesis, in progress, Michigan Tech); in this case, the results are very similar to those produced using the model cited earlier by Bentley et al.]

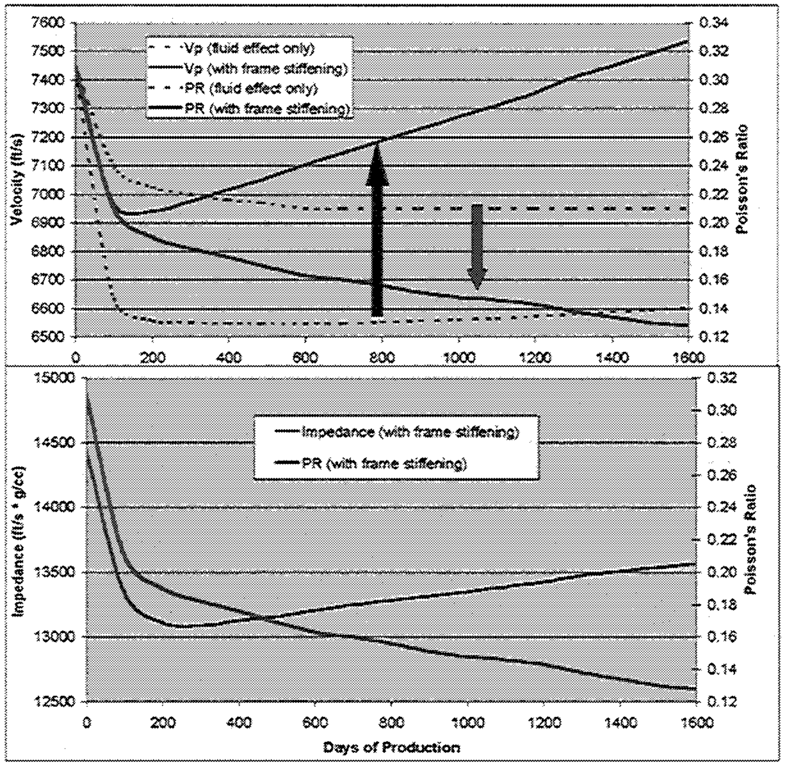

Figure 41: Changes in P-wave velocity (Vp), Poisson's ratio (PR), and Acoustic Impedance with time of production. The upper graph shows Vp and PR as a result of the fluid substitution calculations only (dotted lines) and with the inclusion of frame stiffening effects (solid lines). Notice that the frame stiffening effect eventually more than cancels the reduction in velocity due to the fluid substitution, while enhancing the Poisson's ratio effect. Inclusion of the density changes (oil to gas) decreases the impact of frame stiffening on the impedance results (lower graph), but following an initial dramatic decrease, the impedance increases with time during most of the life of the field.

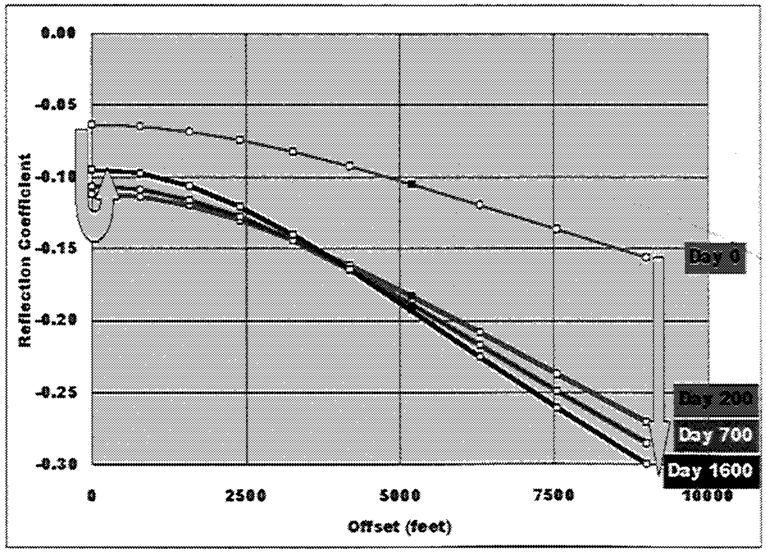

Figure 42: Predictions for Amplitude-versus-Offset effect to be observed in time-lapse data for Teal South. Small squares indicate each additional 5 degrees in angle of incidence, and the black square indicates 30 degrees. Notice that the far offsets are expected to continuously increase in amplitude as production continues, but that the near offsets will initially increase, then subsequently decrease in amplitude. Phase I seismic data was collected about 230 days after production began, and Phase II about 950 days.

PRE-STACK TIME-LAPSE SEISMIC OBSERVATIONS

We chose to investigate the pre-stack behavior of the reflections from the 4500-ft reservoir and from the Little Neighbor reservoir in the OBC data from Phase I (shortly after the initial release of free gas) and Phase II (after a couple years of continued production). Because the seismic traces are not equally distributed among the offset ranges and their distribution varies among cdp gathers, we grouped the offset traces into different ranges and constructed partial stacks within each range. Results are presented here for every fourth cdp gather along one east-west line intersecting both reservoirs, as indicated in Figure 1. The reflections from the 4500-ft reservoir (Figure 43) show that the far offsets increased in amplitude between Phases I and II, while the small-amplitude near-offsets remained essentially constant.

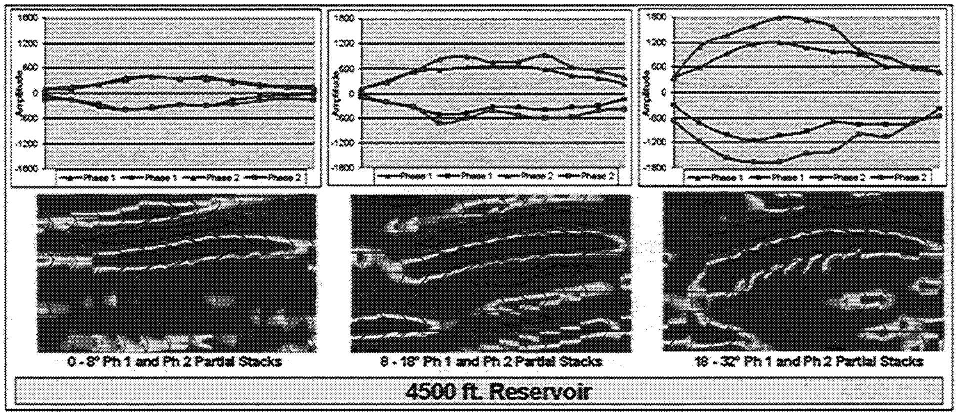

Figure 43: Amplitudes extracted from the partial-offset (unmigrated) stacked seismic P-wave data for the 4500-ft reservoir from Phases I and II (data provided by CGG). The upper diagrams show the amplitudes of each partial-stacked trace, measured on the upper trough and the lower peak as shown on the lower diagrams This figure shows a rough, although not exact, agreement with the model prediction shown in Fig. 42.

The reflections from the "Little Neighbor" reservoir (Figure 44) show that the same situation exists, except that the near-offsets actually decreased slightly in amplitude between the two phases. Both reservoirs show characteristics (within noise limits) of reservoirs that have released free gas, and which continue to increase gas saturation while decreasing reservoir pore pressure.

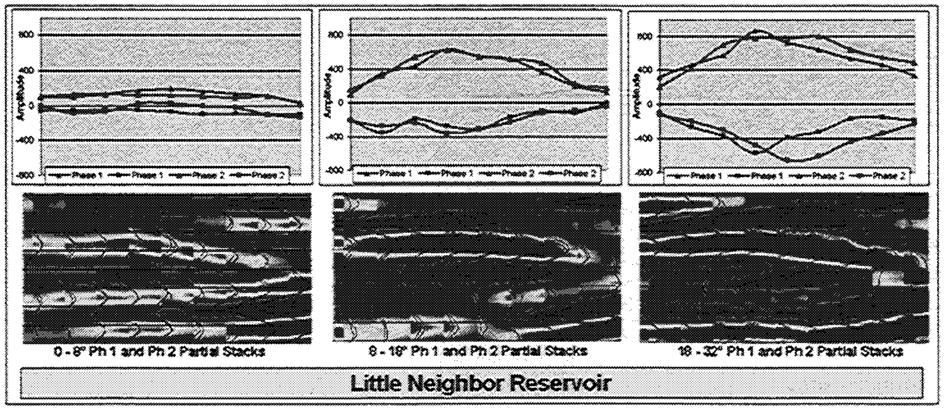

Figure 44: Amplitudes extracted from the partial-offset stacked seismic P-wave data over the Little Neighbor reservoir. Compare with the observations for the 4500-ft reservoir in Figure 43. Note that the near-offsets have decreased in amplitude between Phases I and II, and that the far offsets have increased in amplitude, in very good agreement with the model presented for the expansion of a free gas phase and a decrease in reservoir pressure, even though this reservoir is not being produced.

Interpretation

This behavior contains two surprises for the conventional viewpoint: First, the amplitudes do not monotonically brighten as additional gas is released; instead, the near-offsets eventually decrease (from one time-lapse survey to another after an initial brightening), while the far-offsets increase in amplitude. Second, the Little Neighbor reservoir, originally thought to be separated by sealing faults, is responding to production in the 4500-ft reservoir in a manner that is remarkably similar to the seismic response exhibited by that reservoir. Our conclusion is that the Little Neighbor reservoir is undergoing a decline in pressure due to the production of the 4500-ft reservoir. It must be in pressure communication through some route within the formations for this to occur, and therefore not isolated by the faults which bound either reservoir. By examination of the inverted acoustic impedance volume along an arbitrary seismic path that links the downdip ends of each reservoir, we find that there is indeed a path of continuous (water) sands that connect the two reservoirs, and perhaps others as well (Figure 45).

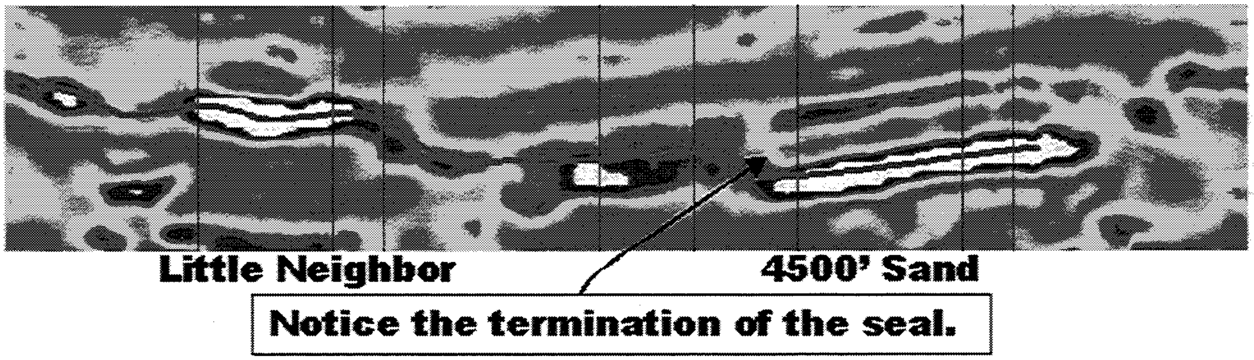

Figure 45: A traverse through the inverted acoustic impedance volume from the legacy data set, connecting the downdip ends of the 4500-ft reservoir and the Little Neighbor reservoir. The ends of the section meet, providing a full circle starting (at the left edge) updip of the Little Neighbor reservoir, with bends in the section at each vertical line, extending, clockwise, through the 4500-ft reservoir, finally returning to the starting point. White is used to highlight the lowest-impedance sands (those likely containing light hydrocarbons); red indicates impedance corresponding to water sands; and green indicates impedance corresponding to shales. Note that the shales form traps, but the each reservoir has its own spill point into water sands; the reservoirs are connected, and in pressure communication, through these spill points.

There are serious implications for reservoir management contained in this interpretation. The fact that the Little Neighbor appears to be in pressure communication and that it exhibits a seismic response appropriate for the creation of a free gas phase results in a volume accommodation problem. The free gas occupies more volume than the oil from which it was released; usually, this volume is more than accounted for by the production of the oil. But in the Little Neighbor's case, the oil contained within it is not being produced. It must be moving down-structure within the formation as the gas cap grows. But downstructure there is no trap to contain it – there is only the spill point (see Figure 46 for a cartoon version of this scenario). The displaced oil of the Little Neighbor reservoir can not migrate to the 4500-ft reservoir and be produced there – that is much too far downstructure, and there are many routes for the oil to escape prior to reaching it. Instead, the oil is likely escaping through the spill point, and either pooling in some other local trap, or escaping into the overlying sands. This oil is likely to be lost for ever, inaccessible to future production, unless it happens to be trapped in some upper zone with economics favorable for recovery. If a well were to be drilled into the Little Neighbor reservoir at this time, the oil in place would be found to be much less than that estimated from the legacy data, obtained prior to production of the nearby 4500-ft reservoir.

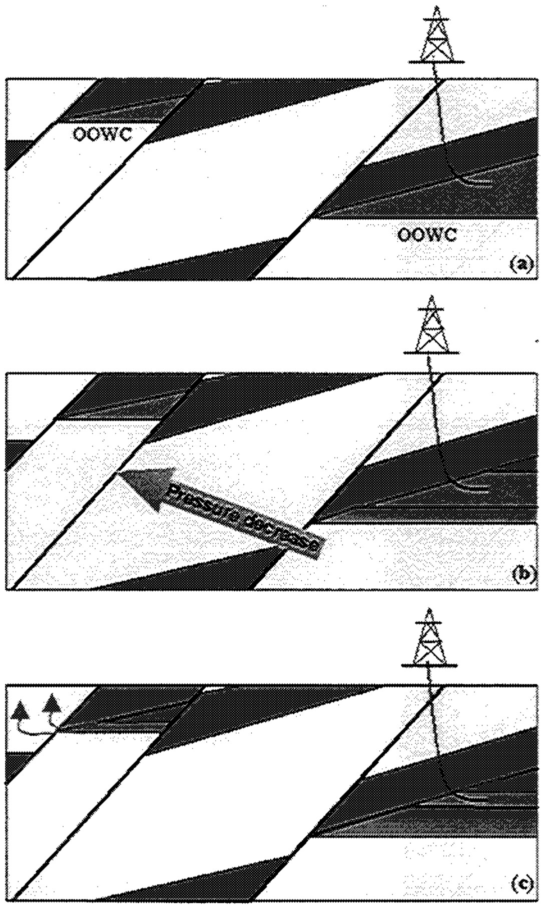

Figure 46: Cartoon schematic of the sequence of events resulting in the loss of hydrocarbons from the Little Neighbor due to production in the 4500-ft reservoir. The 4500-ft reservoir is shown to the right, and the little reservoir is shown to the left, in a geometry similar to that shown along the traverse line of Figure 9. OOWC is the Original Oil Water Contact. In (a), production has just begun in the 4500-ft reservoir, and no displacement has yet been observed. In (b), production from the 4500-ft reservoir has resulted in free gas and water encroachment in that reservoir, as well as a pressure decrease that is communicated through the water sands. In (c), that pressure drop has resulted in the creation of free gas in the Little Neighbor reservoir, and the downward displacement of the remaining oil. That oil eventually spills out of the reservoir, likely never to be recovered.

IMPLICATIONS

The time-lapse survey of Teal South has yielded some completely unexpected results that could be of significant importance for reservoir management of the fields in this block. For this reason, it may not be advisable to design time-lapse surveys to test only one single aspect of production – we feel that our knowledge of the greater reservoir system is, in general, fairly incomplete, and seismic surveys for time-lapse purposes should be designed to allow for the observation of the unexpected. The Teal South experiment was designed in a manner that permitted us to draw the conclusions presented in this paper, which was fortunate. We do not presently know whether the phenomenon observed here – that production in one reservoir is apparently resulting in the loss of hydrocarbons from another unproduced reservoir – are likely to be widespread in the Gulf of Mexico and elsewhere, or not. But we do know that without the time-lapse seismic observations, we would not have recognized it in this instance.

Wamsutter Arch, Wyoming

The fourth field we studied was Wamsutter field, WY, operated by BP (formerly Amoco). Production here is primarily from the Almond formation (mostly gas, some oil) with some additional gas coming from other parts of the section in some areas. This field provided a great challenge: conventional attributes were not known to provide any assistance in identifying potential 'sweetspots' or other productive areas. The field is also near the Siberian Ridge field, the subject of a separate, unrelated, DOE/GRI field study which also found that conventional seismic attributes were of little use. There were several reasons for choosing this field for our final study area. We wanted a site that was would present a challenge to the use of seismic attributes, yet which clearly had wide variation in the production from well to well that was apparently associated with geologic features (and not differences in completion techniques, for example). We also sought a field that presented difficulty in tying seismic data to well log data due to wide velocity variations within thin beds, and this field contained finely interbedded coals and high-velocity sands in order to examine various aspects of upscaling velocity functions. Ideally, our final field study would also provide a good test case for possible pressure compartments, particularly ones that are associated with fine-scale fracturing; although we are not yet certain that these are present in Wamsutter, our study strongly suggests that they are likely. Finally, we sought a field in which the potential to increase production as a result of our study might be possible, although it was not necessarily a specific goal of the original project. The Wamsutter field met all of these objectives, and had good-quality seismic data and sufficient logs in wells spaced throughout the field to allow us to conduct our analysis with some confidence. The one piece of data lacking from the field was a vertical seismic profile (VSP) or checkshot, but we have managed to conduct our upscaling study with some confidence in spite of this shortcoming. Our results demonstrate that the selection of Wamsutter field was appropriate: we have identified unconventional seismic attributes that are convincingly associated with the presence of a sand-bar or barrier-island facies that is also highly productive, and other unconventional attributes that seem to be associated with areas of high fluid pressure and/or dense microfracturing, also areas of higher productivity.

Figure 47 shows the location of the Wamsutter field in Wyoming. It is part of the Green River basin, along the Wamsutter arch. Figure 48 shows an outline of the seismic survey and a bubble plot of first-year production (of gas, in this case) of the wells in the greater area. Two areas of enhanced production are identified in Figure 48.

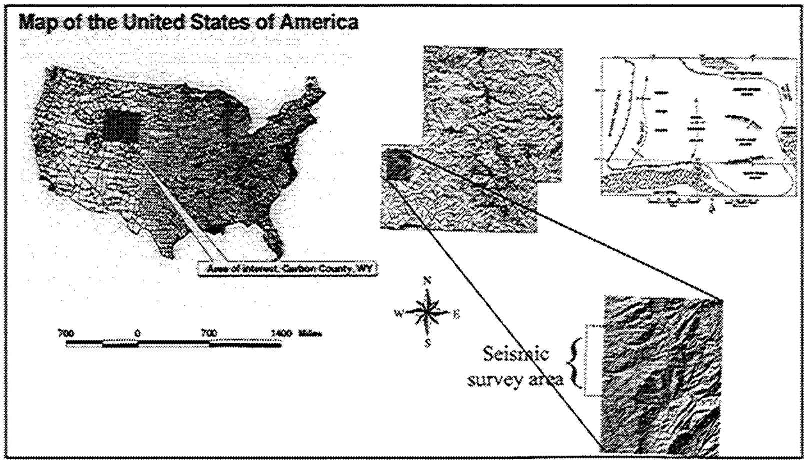

Figure 47. Location maps showing Wamsutter field.

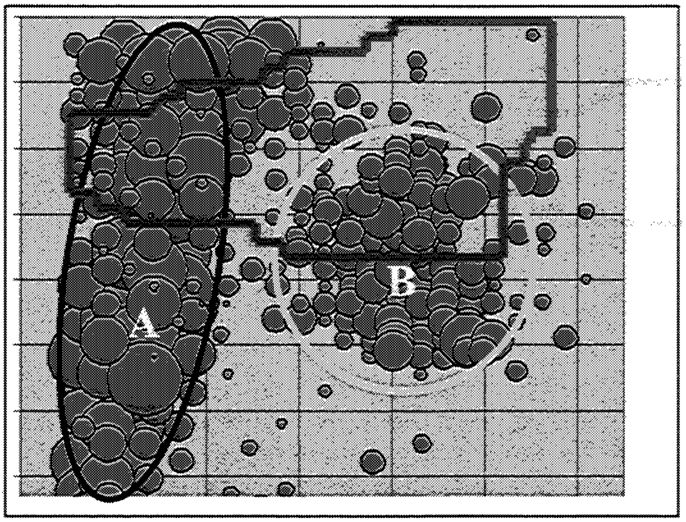

Figure 48: (Approximate) location of the seismic survey (outlined in red) and first-year (gas) production indicated by size of bubbles. Two areas of higher production are readily apparent: the area labeled "A" is associated with a known sand-bar or barrier-island facies at the top of the Almond formation, and the area labeled "B" is associated with moderately enhanced production throughout the section in and near the Almond.

Our analysis included a fairly exhaustive search of conventional seismic attributes, and yielded none which convincingly provided an indication of the productive areas of the field. These are not detailed here, but will be described in future publications and reports. Our efforts then turned to unconventional attributes, using the insight that is afforded by already knowing where the productivity is the greatest, and some limited insight into what geologic features may be responsible for that increased productivity.

The area labeled "A" on Figure 48 is known to be associated with a temporary cessation of a transgressive stage and the associated creation of a sand bar or barrier island at this location. It can be identified on Gamma Ray logs as a thicker interval of very clean sand, yet it present almost no contrast with the overlying Lewis shale in either P-wave velocity or density, and thereby yields no coherent reflection (see Figure 49 for an example of a log suite in the productive sand-bar facies). The 'Top of the Almond' reflection can be identified elsewhere from a contrast in acoustic impedance between the Lewis shale and the unproductive non-sand-bar facies of the Almond. Thus, we could visually identify the sand bar from the seismic data as being present at the locations where the Top Almond reflection was not readily mappable from the seismic data. This is an unsatisfying approach to seismic interpretation, although one that interpreters are forced to make frequently.

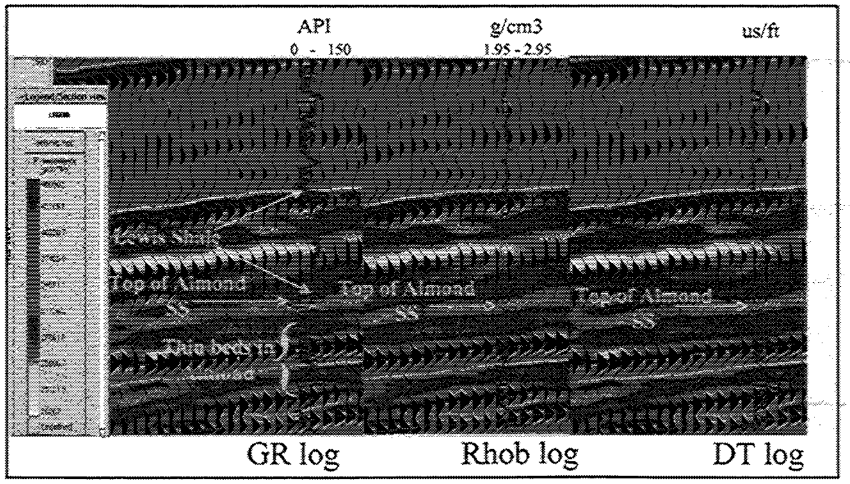

Figure 49: Typical logs of the portion of the Wamsutter field where the sand-bar or barrier-island facies is present; seismic data (repeated for each log) are displayed as wiggle lines, and the background colors indicate acoustic impedance resulting from well-constrained inversion.

SAND BAR IDENTIFICATION: LATERAL INCOHERENCE

We sought a quantifiable and mappable attribute that could easily be used by interpreters to identify the portion of the Top Almond that was occupied by the sand-bar facies. We found that this example provided an excellent application of 'phantom' horizons derived from a widely mappable nearby and conformable horizon (contrary to our experience in the Stratton data set, described elsewhere in this report). In this case, we used the widespread and readily mappable 'Lower Almond' horizon as the basis for creation of a series of phantom horizons. Where the Top Almond horizon could be tracked, it was about 36 ms above the Lower-Almond horizon (see Figure 50).

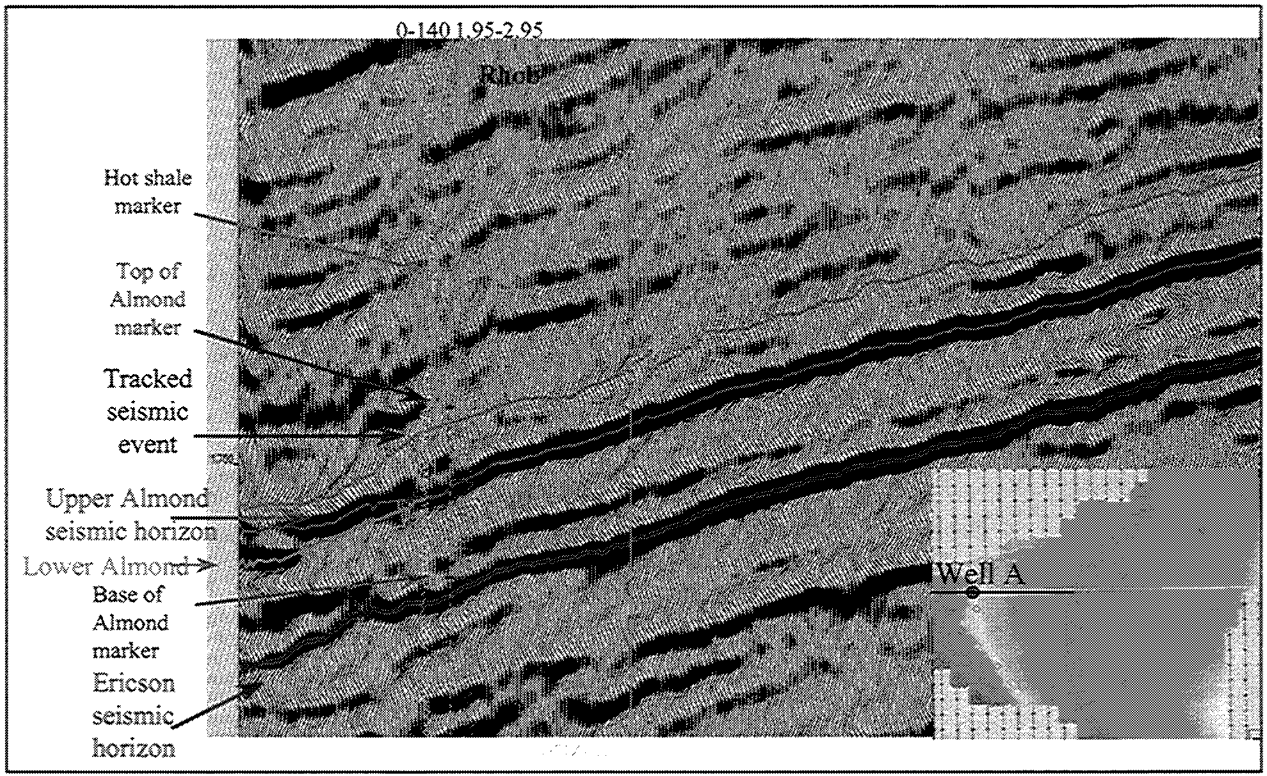

Figure 50: Seismic section in area of the sand-bar or barrier-island facies; note incoherent reflection at location of the sand bar as indicated by 'Top of Almond Marker' from well logs.

We then computed the variance (a sort of incoherence attribute available within the GeoQuest software suite) over several intervals, and found that high levels of variance corresponded very closely to the location of the sand-bar or barrier-island facies as identified from logs and from production (see Figure 51). We feel that this attribute is reliable and robust and could be used further in this and other similar situations. It appears to indicate imbricate or onlapping coastal features that are locally continuous but which terminate abruptly, perhaps associated with contemporaneous sand-bar edges or shorelines.

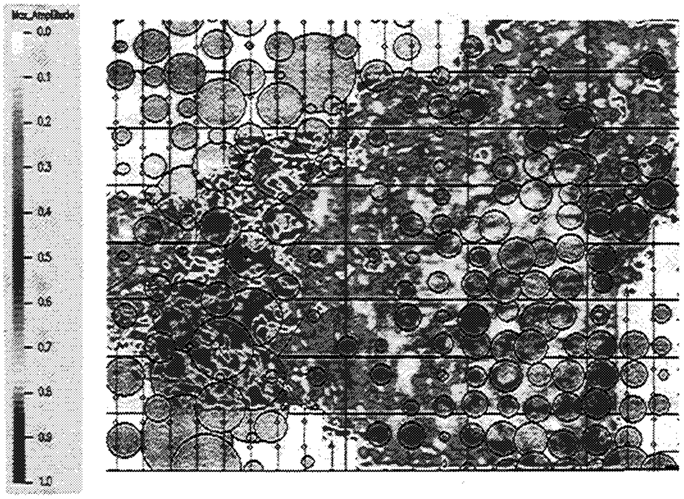

Figure 51: Variance (hot colors indicate a large degree of incoherence) of the seismic data within the interval lying 32-38 ms above the Lower Almond horizon. This attribute seems to accurately identify the sand-bar or barrier-island facies at the top of the Almond formation and is clearly identifying the more-productive region, as shown from the bubble overlay, in the western portion of the survey (area "A" from Figure 48).

FLUID PRESSURES AND MICRO-FRACTURING: DFM AND IMPEDANCE VARIATION

Having satisfied ourselves that we had identified an attribute useful for the delineation of the sand-bar or barrier-island facies at the top of the Almond formation, we turned our attention to the more elusive nature of production in the eastern part of the survey, area "B" in Figure 48. We did not, at the time of our examination of the data, know the perforated intervals from which this production was extracted, but we sought an attribute that would provide information on 'sweetspots' as they are known in this region of the Western US. It has long been suspected that some extent of fracturing and/or pressure differential is responsible for improved production in local areas, termed sweetspots. Simultaneous with our efforts, a separate DOE/GRI study in the nearby Siberian Ridge field was concluding that large fracture networks were not responsible; eventually, that study yielded the result that local pressure compartments were controlling production potential, and that these could be identified by seismic-stacking velocity anomalies consistent with increased pore pressures. We did not have access to pre-stack data nor the stacking velocities associated with processing the seismic data; in any case, we sought attributes that could be used by other interpreters with access to P-wave stacked data only. As part of the project plans, we had the seismic data volume processed by TransSeismic International using their DFM (Dynamic Fluid Method) technology, which we felt was well-suited to identifying micro-fractured intervals and/or high-fluid-pressure regions; we also had performed a well-constrained inversion for acoustic impedance on the data volume using software provided by Jason Geosystems. Both of these techniques yielded results which seem to support the model that enhanced production in area "B" is caused by an increase in fluid pressure and/or an associated increased density of microfracturing. The DFM approach (described in previous reports and in a paper published by Pisetski in THE LEADING EDGE in September, 1999) makes use of the instantaneous amplitude and instantaneous frequency attributes in a way that removes the effects of stratigraphic changes in those parameters. Inversion for acoustic impedance uses amplitudes of reflections to determine the reflection coefficient and, by integrating, the acoustic impedance (after merging with long-wavelength information provided by well logs).

We added one additional aspect to the acoustic inversion process, inspired by our understanding of some versions of the DFM process: we tracked a number of horizons within the section of interest (the uppermost Almond and the overlying Lewis intervals, see Figure 52) and divided the section into a number of very thin intervals; we then sought the lowest-impedance zones along each thin interval, and identified that as a new 'body', collecting these bodies along all the intervals.

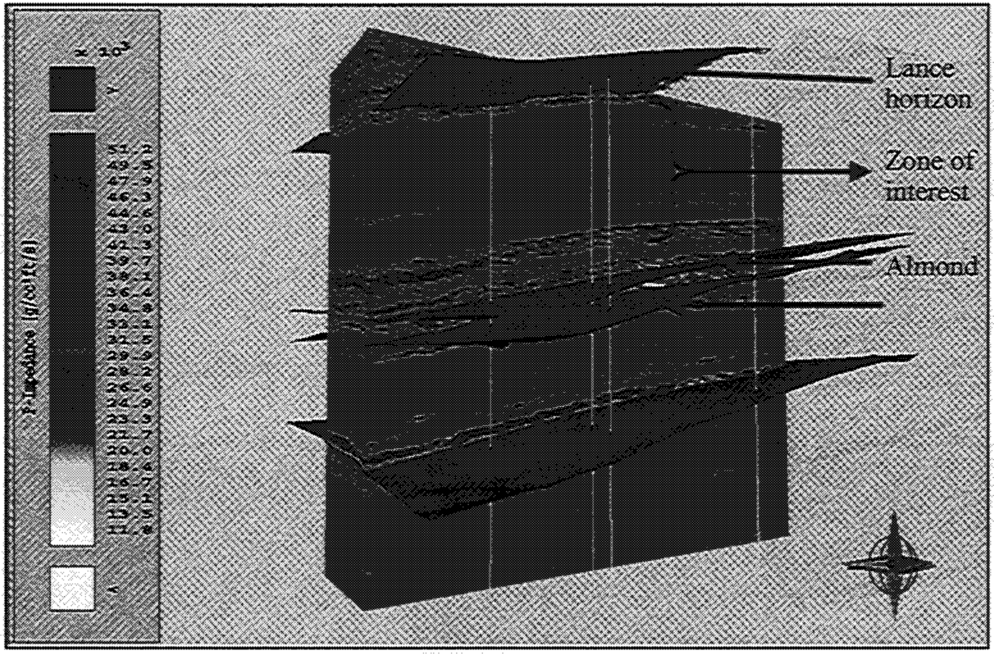

Figure 52: Identification of zone investigated for lower acoustic impedances, identified within thin intervals of coals, sands, or shales; background color indicates acoustic impedance.

Our intention was to remove the stratigraphic differences in acoustic impedance that result simply from changes in lithology; if the lithology was constant along a thin interval or horizon, however, any lower impedance region of that interval may be due to increased fluid pressure and/or increased density of microfracturing. Thus, we could use intervals of coals and intervals of low-porosity sands, and, in each, find the lower-impedance regions without concern for the fact that the coals were everywhere lower impedance than the sands. We collected these low-impedance bodies within the volume and compared them with known production (see Figure 53)

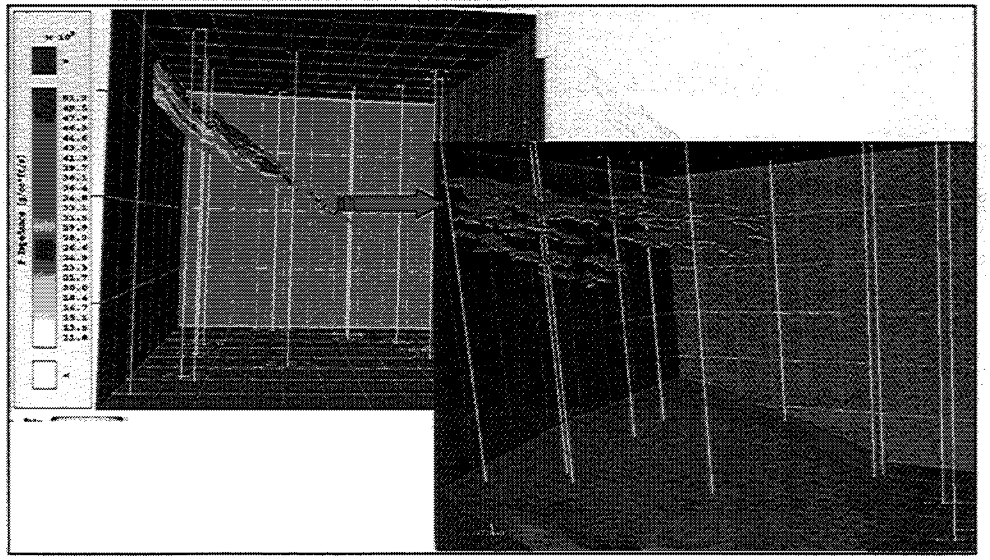

Figure 53: On left, thin interval of the acoustic impedance volume, from which low-impedance zones are extracted as individual bodies; on right, compilation of these low-impedance bodies from a large number of thin intervals.

We then summed the separate thicknesses of these bodies in order to create a map of net low-impedance volume concentrations (using a proxy value, 'netpay', readily available in the software suite employed); the results are displayed later in comparison with the DFM results.

The DFM processing of the Wamsutter data was the most interesting of the main data sets processed by this technique, perhaps because this data volume is, in our opinion, the most appropriate for that technology. In order to make the analysis of the DFM results interpretable in terms of comparison with production, we isolated a large number of individual 'bodies' within the DFM volume with values appropriate indicative of high fluid pressure and/or increased fracture density (see Figure 54).

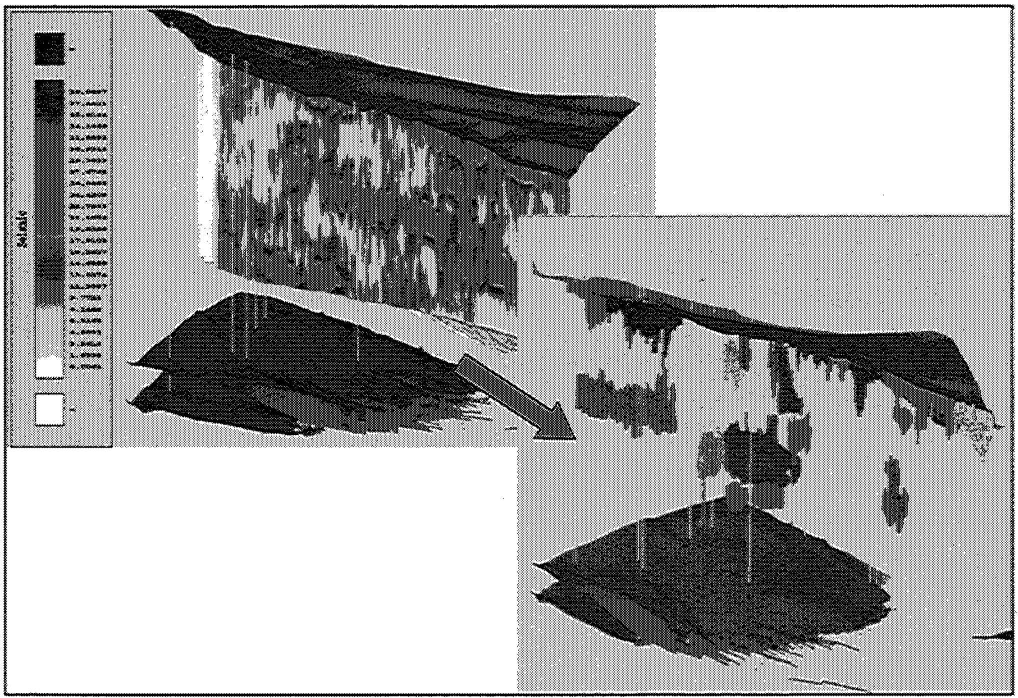

Figure 54: On left, a view of the DFM volume; values of DFM that are suggestive of high fluid pressure and/or more intense microfracturing are indicated by the cooler colors (blue and green); on right, identification of a number of specific bodies extracted from the DFM volume.

Both the DFM and the processed inversion results yielded results that strongly suggest they can be used for identifying the higher-production "sweetspots" such as that identified in region "B". Figure 55 shows a comparison of the RMS amplitude (over an interval from the Lower Almond horizon to 70 ms above this horizon), the processed inversion results (by using the 'netpay' proxy for total accumulated thickness of lower-than-typical impedance along each thin interval), and the summed DFM results (by adding together the thicknesses of each body at each map point). These results should be compared with the detailed first-year production as shown in Figure 51; they agree very well, although RMS amplitude provides the weakest correlation, indicating the added value of the DFM and the processed inversion techniques.

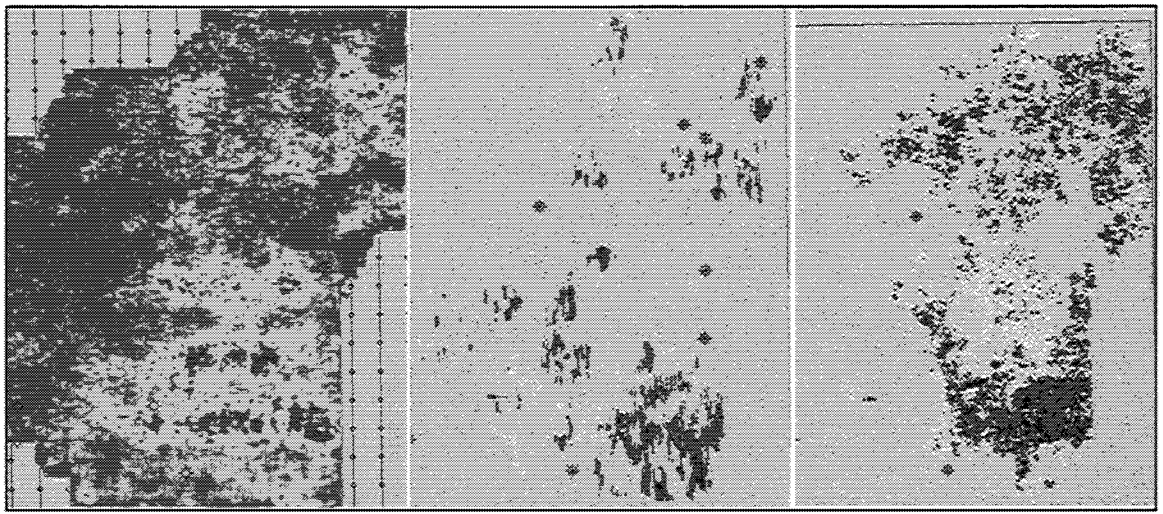

Figure 55: Comparison of RMS amplitudes (left), processed acoustic-impedance results (center), and DFM analysis (right). Compare the locations indicated in each of these maps with the production data from Figure 51.

It may be a remarkable coincidence that most of the wells for which we have good log data, as indicated by the well symbols on Figure 55, tend not to lie within the apparent highest-potential areas as shown by the coloring in that figure. Other wells, for which first-year production data are available, as indicated in Figure 51, support the interpretation that the DFM and processed inversion results indicate the sweetspot, but the absence of well data in those zones hampers our interpretation somewhat. The contrast may, however, be related to production effects.

UPSCALING AND BACKUS AVERAGING

The final aspect of our investigation of Wamsutter field involves the upscaling of the high-contrast thin layers from logging scale to seismic scale; this work is currently being completed, but the main results are now clear and can be reported here. The response of a seismic wave to thin layers of alternating high and low velocities is known to be inaccurately represented by the typical (ray-theoretical) time-average of the sonic transit time as indicated by short-spacing, high-frequency (in comparison with seismic) sonic logging tools. The 'correct' averaging is often referred to as Backus averaging, named after the author (George Backus) of a fundamental paper on the subject. It is equivalent to the low-frequency limit of the O'Doherty-Anstey model, or to other 'effective medium theory' approaches designed for layered media. We investigated the one-dimensional Backus average approach to upscaling sonic logs with the intention of providing sound guidelines for routine application within synthetic-seismogram generation routines. The main effect of Backus averaging is to average the compliances of the formations, rather than their slownesses; in the one-dimensional P-wave case, that corresponds to averaging the uniaxial compressibility, and is proportional to the inverse of the square of the velocity, resulting in an increased significance of the lower-velocity layers at the expense of the higher-velocity ones. Thus, in the Wamsutter case, the thin low-velocity coal layers (see Figure 56) have a greater effect in the Backus-averaged (upscaled) log than in the conventional sonic log as used for synthetics generation. We investigated a number of approaches to performing a windowed Backus average and their effects on the resultant drift curve and synthetic seismograms.

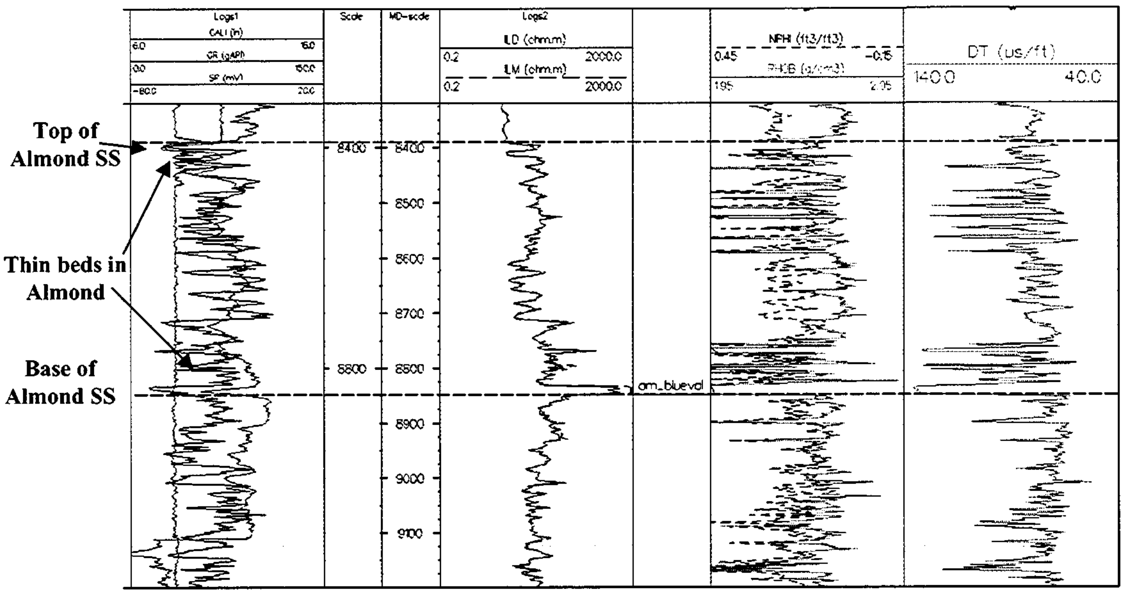

Figure 56: Example of a log suite from Wamsutter field showing the thin-bedded coals (identified by low RHOB values, less than 1.95), sands (low GR values not corresponding to coals), and shales (high GR values and NPHI-RHOB separation). The "Base of Almond SS" is identified by the thick coal unit (also labeled "am_blueval"), and lies just above the top of the Ericson sandstone. This marker is associated with a strong reflection, referred to as the top of the Ericson.

The values of DT and RHOB obtained in many of the wells are in good agreement with core data from other coals and with other logged coals; we tend to feel that the values logged are generally good, and, when they are not good, the usual bad-hole indicators apply. We selected one well with particularly good density and sonic log data for our detailed study of upscaling using Backus averaging.

For ease of demonstration, we present in Figure 57 a comparison of the original sonic log and the Backus-averaged log using a 400-ft moving window. Notice that the averaged log exhibits, as expected, a much more slowly varying character than the original log. We used this and other time-window-length functions to provide new time-depth relationships, the most-important aspect of upscaling. The 'drift' curves, comparing the difference in time (for each point in depth) between the upscaled and conventional ties, are compared for different window lengths, also shown in Figure 57. The 'tie point' has been set at the top of the Ericson, rather than at the surface of the earth or at the seismic datum.

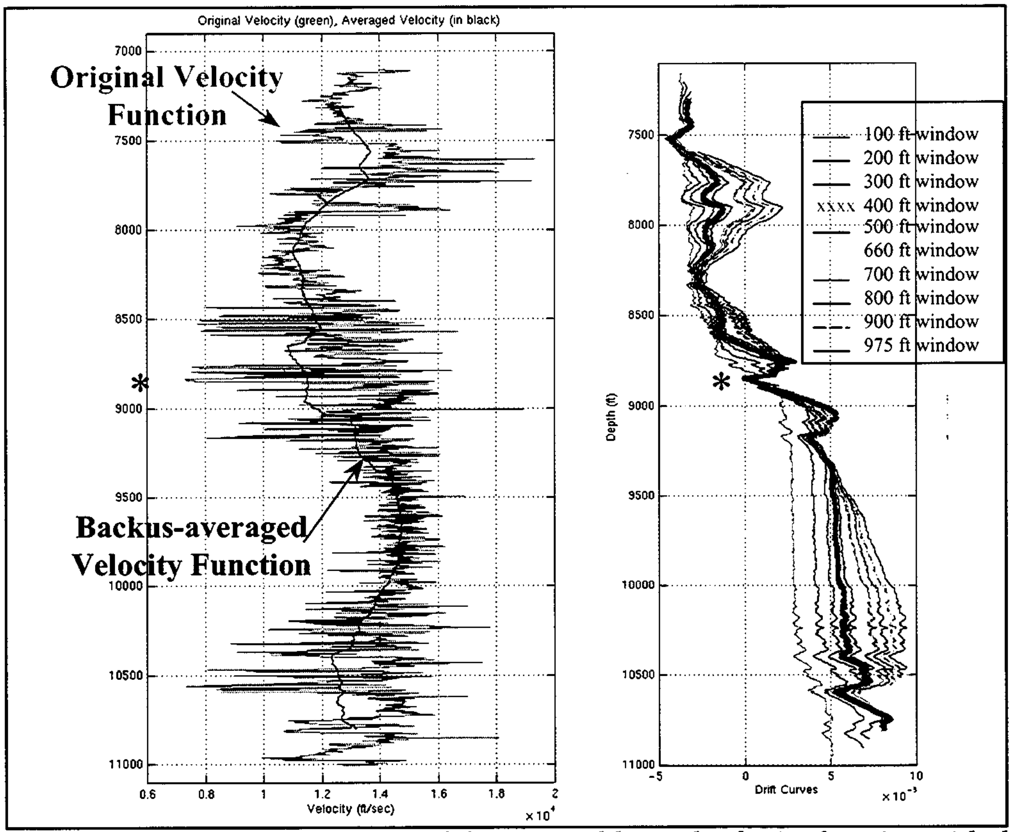

Figure 57: Left side shows a comparison of the original logged velocity function with the Backus-averaged log using a window length of 400 ft. Right side shows a comparison of drift curves for different window lengths, as indicated in the legend. The 'tie' point at the top of the Ericson is indicated by the asterisk, and all drift curves must be zero at this depth.

In the absence of a reliable checkshot or VSP survey, the interpreter is often faced with this same condition: one seismic horizon is unambiguously identifiable as associated with a log marker or formation top, but the other seismic events are not so clearly associated, and some 'stretching and squeezing' is usually applied, often without much thought, to accomplish the tie. It is this subjective step that we wish to reduce in uncertainty by performing a quantifiable and theoretically justified upscaling.

Figure 58 shows one of our final (to date) results, a comparison between the synthetic seismogram generated by conventional algorithms and one generated after Backus-average upscaling. In this case, we applied a time-depth function derived from a 500-ft time window for moving averaging, and then used a value for velocity at each time (or depth) that was 'corrected' to a 'high-fidelity' ('Hi-Fi') value by multiplying it by the ratio of the time-averaged velocity and the Backus-averaged velocity at each depth (using the same time-window for both averages). We see that the tie has improved significantly, and that the correlation coefficient has also improved, from 0.59 to 0.72. Our future work required to complete this portion of the project will involve using much finer time windows than we have investigated so far.

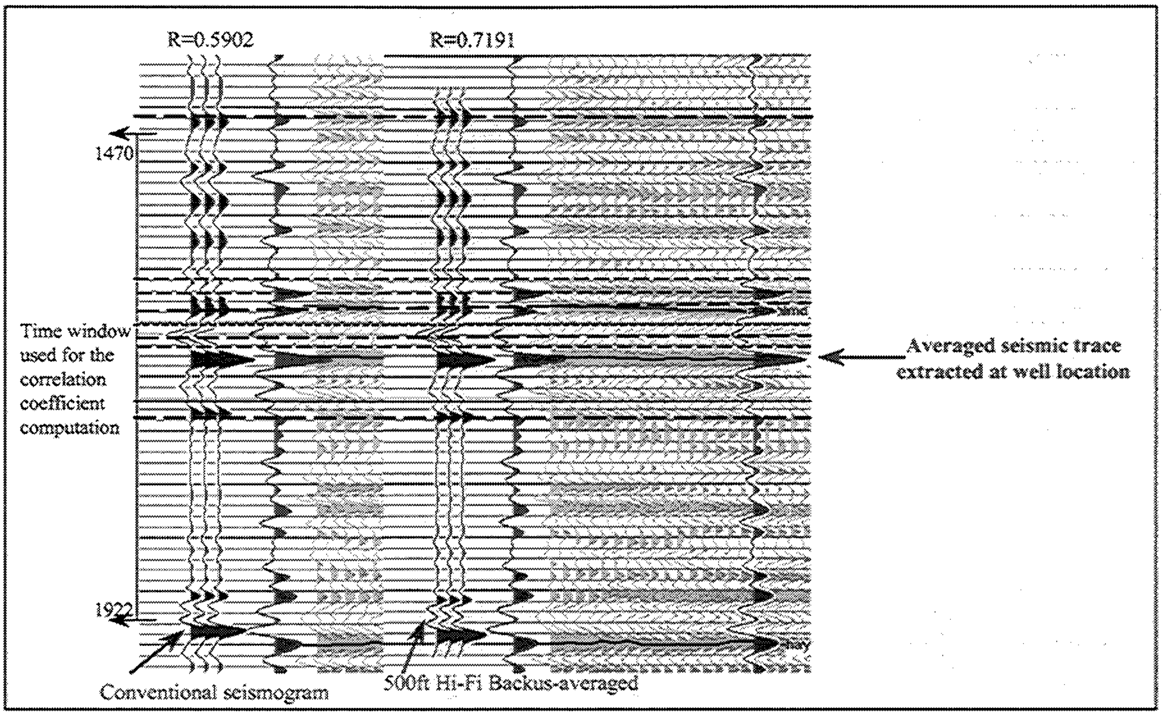

Figure 58: Comparison of conventional synthetic seismogram with our Hi-Fi Backus averaged (500-ft window) synthetic seismogram. Notice that the fit has improved considerably.

Summary of Attribute Characteristics

This study has provided new results in the following particular aspects of seismic attributes:

- The use of phantom horizons
  - Pitfalls (from the Stratton study)
  - Recommended usage (lateral incoherence, from the Wamsutter study)
- The value of impedance
  - For predicting time-lapse response (Teal South study)
  - For calibrating in the absence of good log data (Teal South study)
  - Alternate methods of computation (Boonsville study)
  - Pitfalls when beds are thin (Boonsville study)
  - Use (lateral variations) for predicting fluid pressures and/or microfracturing (Wamsutter)
- Attributes designed to meet the need, recognized from rock physics
  - Lateral incoherence (Wamsutter)
  - Lateral variations in impedance (Wamsutter, Boonsville)
  - Dynamic Fluid Method (from TransSeismic International)
  - Facies analysis (existing methods, Boonsville)
  - Quantitative Facies Analysis (new method, Boonsville study)
- Upscaling to seismic and reservoir scales
  - Backus averaging (Wamsutter)
  - Pitfalls and sensitivity (Boonsville)
- Implications for reservoir management
  - Time-lapse monitoring including pressure dependence (Teal South)
  - Natural pressure variations (Wamsutter)

Conclusions

The project, "Calibration of Seismic Attributes for Reservoir Characterization," is on schedule as planned. We have studied four fields rather than the three initially promised, and are using more sophisticated software suites than initially planned. The analysis of the data sets is essentially complete and we are concentrating on the tech transfer component.

We have found several specific aspects of attributes that may be generally unrecognized among interpreters in the field. These are itemized in the previous section, and include: the use of phantom horizons ,the value of impedance, the design of attribute analysis to meet specific needs, methods of facies analysis, upscaling, and implications of several observations to reservoir management. Our results have direct bearing on thin-bed environments, time-lapse seismic monitoring, and areas in which attributes have conventionally been of little application.

Acknowledgments

The Energy Research Clearing House, particularly Roger Entralgo and Gene Sparkman, and the members of its Teal South 4D-4C consortium, provided the Teal South data and helpful discussions. Preliminary models were aided by advice provided by J. Ashbaugh and P. Flemings of Penn State. Legacy streamer data was provided by Diamond Geophysical, and Phase I and Phase II data was provided by CGG; W. Haggard and S. Spitz provided additional details and specially formatted data for our use. Assistance in performing the inversion for acoustic impedance was provided by B. Rees and D. Graham of Jason Geosystems.

BP and its predecessors have generously provided the Wamsutter data set for our use, and have been extremely helpful in discussions and advice. We gratefully acknowledge their support of this project.

Software used in this project has been graciously provided by Landmark Graphics, Jason Geosystems, Schlumberger-GeoQuest, Hampson-Russell, Paradigm, Scott-Pickford, Mercury International, Paradigm Geophysical, and GXTechnology.

All interpretations presented in this report are those of the authors, and not necessarily those of the people or companies that support this research. Responsibility for all errors rests with the authors. [Additional disclaimer is presented at the start of this report.]

References

Batzle, M. and Wang, Z., 1992, Seismic properties of pore fluids, Geophysics, 57, 1396-1408.

Backus, G, 1962, Long-wave elastic anisotropy in transversely isotropic media: Geophysics, v. 44, p. 896-917.

Bahorich M. and, S. Farmer, 1995, 3-D seismic discontinuity for faults and stratigraphic features: the coherence cube: The Leading Edge, v. 14, p. 1053-1058.

Brown, A. R., 1996, Interpretation of 3-D seismic data (4th edition): AAPG Memoir 42, published by AAPG, Tulsa, OK.

Carr, D. L., R. A. Johns, and R. Y. Elphick, 1997, High-resolution reservoir characterization of midcontinent sandstones using wireline resistivity imaging in Boonsville (Bend Conglomerate) gas field, Fort Worth basin, Texas: The Log Analyst, v. 38, n. 5, p. 54- 69.

Chen C., 1996, Fuzzy logic and neural network handbook, McGraw-Hill, Inc.

Chen, Q. and S. Sidney, 1997, Seismic attribute technology for reservoir forecasting and monitoring, The Leading Edge, May, p. 445-456.

Chi, C., J. Mendel, and D. Hampson, 1984, A computationally fast approach to maximum-likelihood deconvolution: Geophysics, v. 49, v. 5, p. 550-565.

Chopra, S., 2001, Integrating coherence cube imaging and seismic inversion, The Leading Edge, April, p. 354-362.

Coleman, J. M. and D. B. Prior, 1982, Delta environments of deposition, in Sandstone depositional environments edited by P. A. Scholle and D. Spearing, published by AAPG, Tulsa, OK, p. 139-170.

Cooke, D. and W. A. Schneider, 1983, Generalized linear inversion of reflection seismic data: Geophysics, v. 48, n. 6, p. 665-676.

Cooke, D., A. Sena, and G. O'Donnell, T. Muryanto, and V. Ball, 1999, What is the best Seismic attribute for quantitative seismic reservoir characterization?: SEG 1999 Expanded Abstract.

Ebrom, D., P. Krail, D. Ridyard, and L. Scott, 1998, 4-C/4-D at Teal South, THE LEADING EDGE.

Emery, D. and K. Myers, 1996, Sequence stratigraphy, published by Blackwell Science Ltd., p. 61- 177.

Gastaldi, C., D. Roy, P. Doyen, and L. Den Boer, 1998, Using Bayesian simulations to predict reservoir thickness under tuning conditions: The Leading Edge, n. 4, p. 589- 593.

Glover, G., 1982, A study of the Bend Conglomerate in S. E. Maryetta area, Boonsville field, Jack county, Texas: Petroleum Geology of the Fort Worth basin and Bend Arch area, edited by C. A. Martin, Dallas Geological Society, p. 353-354.

Gurney, K. and Wright M., 1992, A self-organizing neural network model of image velocity encoding, in Biological Cybernetics, v. 68, p.173-181.

Hardage, B. A., R. A. Levey, and V. Pendleton, etc., 1994, A 3-D seismic case history evaluating fluvially deposited thin-bed reservoirs in a gas-producing property: Geophysics, v. 59, n. 11, p. 1650-1665.

Hardage, B. A., R. A. Levey, V. Pendleton, 1994, A 3-D seismic case history evaluating fluvially deposited thin-bed reservoirs in a gas-producing property, GEOPHYSICS, v. 59, n.11, pp 1650-1665.

Hardage, B. A., J. L. Simmons, and Jr. D. E. Lancaster, etc., 1996a, Boonsville 3-D seismic data set: a technology transfer product generated as part of the secondary gas recovery project (GRI-96/0182).

Hardage, B. A., D. L. Carr, D. E. Lancaster, et al., 1996b, 3-D seismic imaging and seismic attribute analysis of generic sequence deposited in low-accommodation conditions, 1996: Geophysics, v. 61, n. 5, p.1351-1362.

Hardage, B. A., D. L. Carr, D. E. Lancaster, et al.., 1996c, Secondary natural gas recovery: targeted applications for infield reservoir growth in midcontinent reservoirs, Boonsville field, Fort Worth basin, Texas: Gas Research Institute, Topical Report(GRI-95/0454.1-2), v. I and v. II.

Hoover, A. R., T. Burkhart, and P. B. Flemings, 1999, Reservoir and production analysis of the K40 sand, south Timbalier 295, offshore Louisiana, with comparison to time- lapse (4-D) seismic results: AAPG, Bulletin, v. 83, n. 10, p. 1624-1641.

Horkowitz, K. O., and D. R. Davis, 1996, Seismic delineation of thin sandstone reservoirs in a shale-rich sequence using instantaneous frequency and reflection amplitude attributes from 3-D data, Texas Gulf Coast, in AAPG Studies in Geology no. 42 and SEG Geophysical Development Series No. 5, edited by P. Weimer and T. L. Davis, AAPG/SEG, Tulsa, OK., p. 35-44.

Kohonen, T. 1990, Self-organizing map, Proceedings of the EEE, v.78, n.9, p.1464-1480.

Lahti, V. R. and W. F. Huber, 1982, The Atoka group (Pennsylvanian) of the Boonsville field area, north-central Texas: Petroleum Geology of the Fort Worth basin and Bend Arch area, edited by C. A. Martin, Dallas Geological Society, p. 377-399.

Liu Z. and J. Liu, 1998, Seismic-controlled nonlinear extrapolation of well parameters using neural networks: Geophysics, v. 63, n. 6, p. 2035-2041.

Marfurt K., R. Kirlin, S. Farmer and M. Bahorich, 1998, 3-D seismic attributes using a semblance-based coherency algorithm: Geophysics, v. 63, n. 4, p. 1150-1165.

Marfurt K., V. Sudhaker, A. Gersztenkorn, K. Crawford, and S. Nissen, 1999, Coherency calculations in the presence of structural dip: Geophysics, v. 64, n. 1, p. 104-111.

Michelena, R. J., E. Gonzalez S., and M. Capello De P. 1998, Similarity analysis: A new tool to summarize seismic attributes information: The Leading Edge, v.17, n. 4, p. 545-548.

Oldenburg, D. W., T. Scheuer and S. Levy, Recovery of the acoustic impedance from reflection seismograms: Geophysics, v. 48, n. 10, p. 1318-1337.

Partyka, G., J. Gridley, and J. Lopez, 1999, Interpretational applications of spectral decomposition in reservoir characterization: The Leading Edge, vol. 18, p. 353-360.

Pennington, W. D., 2001, Reservoir geophysics, Geophysics, vol. 60, no. 1, p. 25-30.

Poupon, M., K. Azbel, and J. Ingram, 1999, Integrating seismic facies and petro-acoustic moldering: World Oil magazine, June 1999, p. 75-80.

Riel, P., 2000, The past, present, and future of quantitative reservoir characterization: The Leading Edge, no. 8, p. 878-881.

Russell B., 1988, Introduction to seismic inversion methods, S. N. Domenico, Series Editor Course Notes Series, Volume 2 (an SEG continuing education short course).

Salleh M. S. and S. Ronghe, Reservoir characterization on thin sands in south west Ampa 21 area (BLK11) using seismic inversion: SEG 1999 Expanded Abstracts.

Taylor, H, S. Banks, and J. McCoy, 1979, Deconvolution with the L1 norm: Geophysics, v. 44, p. 39-52.

Thompson, D. M., 1982, Atoka Group (Lower to Middle Pennsylvanian), Northern Fort Worth basin, Texas: Terrigenous depositional system, diagenesis, and reservoir distribution and quality (Investigation report No. 125).

Torres-Verdin C., M. Victoria, G., Merlrtin, and J. Pendrel, 1999, Trace-based and geostatistical inversion of 3-D seismic for thin-sand delineation: an application to San Jorge Basin, Argentina: SEG 1999 Expanded Abstracts.

Widess, M. B., 1973, How thin is a thin bed? Geophysics, v. 38, p. 1176-1180.

Yilmaz, O., 1987, Seismic data processing; published by SEG, (Investigations in Geophysics, Volume 2), Tulsa, OK.

List of Acronyms and Abbreviations

2D---------------Two dimensional

3D---------------Three dimensional

AAPG -----------American Association of Petroleum Geologists

BEG--------------University of Texas Bureau of Economic Geology

CMP -------------Common Mid-Point

DOE -------------United States Department of Energy

DFM -------------Dynamic Fluid Method

ERCH------------Energy Research Clearing House

MTU -------------Michigan Technological University *or* Michigan Tech

NMO-------------Normal Move-out

SEG--------------Society of Exploration Geophysicists

USA--------------United States of America